

Spatio-temporal dynamics in a diffusive Bazykin model: effects of group defense and prey-taxis

Subrata Dey, Malay Banerjee, S. Ghorai*

Department of Mathematics and Statistics, IIT Kanpur, India

E-mails: subratad@iitk.ac.in, malayb@iitk.ac.in, sghorai@iitk.ac.in

Abstract

Mathematical modeling and analysis of spatial-temporal population distributions of interacting species have gained significant attention in biology and ecology in recent times. In this work, we investigate a Bazykin-type prey-predator model with a non-monotonic functional response to account for the group defense among the prey population. Various local and global bifurcations are identified in the temporal model. Depending on the parameter values and initial conditions, the temporal model can exhibit long stationary or oscillatory transient states due to the presence of a local saddle-node bifurcation or a global saddle-node bifurcation of limit cycles, respectively. We further incorporate the movement of the populations consisting of a diffusive flux modelling random motion and an advective flux modelling group defense-induced prey-taxis of the predator population. The global existence and boundedness of the spatio-temporal solutions are established using L^p - L^q estimate. We also demonstrate the existence of a non-homogeneous stationary solution near the Turing thresholds using weakly nonlinear analysis. A few interesting phenomena, which include extinction inside the Turing region, long stationary transient state, and non-homogeneous oscillatory solutions inside the Hopf region, are also identified.

Keywords Group defense; Prey-taxis; Pattern formation; Steady state; Amplitude equation; Bifurcation analysis; Transient dynamics

Mathematics Subject Classification 34C23; 35B32, 35B35, 35K57, 92D40

1 Introduction

Understanding complex dynamics of predator-prey interactions through mathematical modelling is a key topic in evolutionary biology and ecology. Since the seminal work of Lotka [1] and Volterra [2], mathematical models have been developed to explore a diverse range of complex ecological phenomena that include Allee effects [3], group defense [4], hunting cooperation [5], intra-guild predation [6], any many others[7]. The incorporation of the movement of the population makes these models more realistic in the field of spatial ecology [8]. The movement of a population can be due to various reasons. The main reasons include the random motion of individuals and the directed motion of individuals in response to the gradient of some signals, among others. The first one is modelled using a diffusive flux and the latter one uses an advective flux in which the velocity field depends on the gradient of the signal.

*Corresponding author

Let $N(T)$ and $P(T)$ respectively be the densities of the prey and predator populations at time T . The Bazykin type prey-predator model [9, 10, 11], which incorporates intra-species competition among predators, is given by:

$$\frac{dN}{dT} = NG(N) - F(N)P, \quad (1a)$$

$$\frac{dP}{dT} = \zeta F(N)P - \gamma P - \delta P^2, \quad (1b)$$

where $G(N)$ denotes the per capita growth rate of the prey species, $F(N)$ is the prey-dependent functional response and ζ is the conversion coefficient. Further, γ and δ respectively denote the natural mortality rate and intra-species competition of the predator population.

The prey-predator interaction is completely reliant on the functional response function $F(N)$. Therefore, the selection of an appropriate functional response is critical in determining the outcome of the predator-prey dynamics. The literature commonly favors strictly monotonic functional responses that increase with prey density with a finite upper bound, such as $\frac{\alpha N}{1 + \beta N}$ (Holling type-II) [12], $\frac{\alpha N^2}{1 + \beta N^2}$ (Holling type-III) [13], $\alpha(1 - e^{-\beta N})$ (Ivelev) [14], $\frac{\alpha N^2}{1 + \mu N + \beta N^2}$ (Sigmoidal) [15], and $\alpha \tanh(\beta N)$ (hyperbolic tangent) [16]. However, experimental and observational evidence suggest that the assumption of monotonicity in the functional response is not always valid. For example, the experiment by Andrews [17] in microbial dynamics suggests that higher nutrient concentrations can result in an inhibitory effect on microorganisms, which can be modelled using Monod–Haldane function $F(N) = \frac{\alpha N}{1 + \mu N + \beta N^2}$. Sokol and Howell [18] conducted a study on the uptake of phenol by *Pseudomonas putida* in continuous culture, where they found that a simplified form of the Monod-Haldane function, $F(N) = \frac{\alpha N}{1 + \beta N^2}$, provided a better fit to their experimental data. The main characterization of the non-monotonic functional response is that there exists a N_m , such that

$$F'(N) = \begin{cases} \geq 0 & \text{for } 0 \leq N \leq N_m, \\ < 0 & \text{for } N > N_m, \end{cases} \quad \text{and } F(N) \rightarrow 0 \text{ as } N \rightarrow \infty. \quad (2)$$

Group defense refers to the ability of the prey species to defend or conceal themselves more effectively, leading to a reduction or complete prevention of predation when their population size is sufficiently large [19, 20]. Tener [21] provided a clear example of this phenomenon in which lone musk oxen are vulnerable to wolf attacks, while small herds of two to six oxen are occasionally attacked, but larger herds are never successfully attacked. This same pattern was also observed by Holmes and Bethel [22] in their study of insect populations, where large swarms of insects made it difficult for predators to identify individual prey. Clearly, group defense can be incorporated into a prey-predator system using a non-monotonic functional response.

Here, we consider a Bazykin prey-predator model with a logistic growth rate for the prey species and a simplified form of the Monod-Haldane function, $F(N) = \frac{\alpha N}{1 + \beta N^2}$, for the functional response. The governing equations are

$$\frac{dN}{dT} = N(\sigma - \eta N) - \frac{\alpha NP}{1 + \beta N^2}, \quad (3a)$$

$$\frac{dP}{dT} = \frac{\zeta \alpha NP}{1 + \beta N^2} - \gamma P - \delta P^2, \quad (3b)$$

where σ and η respectively represent the intrinsic growth rate and intra-species competition of the prey species.

Self-organized spatio-temporal pattern formation is a fundamental process that plays a critical role in comprehending diverse intricate ecological phenomena in nature. The pioneering work of Turing on chemical morphogenesis [23] has played a pivotal role in advancing our understanding of pattern formation using the reaction-diffusion (RD) theory. RD models have since been extensively studied to explain the formation of patterns in various complex biological systems such as fish skin [24], mussel bed distribution [25], insect wings [26], predator-prey interactions [27], terrestrial vegetation [28], and many others [8]. Spatial Turing and temporal Hopf instabilities are key mechanisms in the development of spatio-temporal patterns. The diffusion-driven Turing instability takes place when a small amplitude spatial perturbation about a stable homogeneous steady-state becomes unstable, resulting in stationary patterns like stripes, spots, or a mixture of both [29, 30]. In addition to stationary patterns, various dynamic patterns that include traveling waves, periodic traveling waves, target patterns, spiral patterns, quasi-periodic spatial patterns, and even spatio-temporal chaotic patterns are typically found due to the Hopf instability and Turing-Hopf instability [31, 32].

The diffusion mechanism corresponds to the random movement of species from a higher concentration area to a lower concentration area. On the other hand, taxis is a directional movement of species in response to a particular stimulus, such as phototaxis due to light [33, 34] and chemotaxis due to chemical gradients [35, 36]. Taxis allows species to move towards or away from their stimulus and it is critical in many ecological processes, including foraging, mating, migration, photosynthesis, and dispersal [33, 35, 37]. There are two types of taxis in a prey-predator system depending on the movement of species [38]. The directional movement of predator species in response to the prey density is called prey-taxis and the opposite is called predator-taxis. These types of taxis-based movements play a significant role in the formation of complex spatial patterns [38, 39, 40, 41]. A RD model with Rosenzweig–MacArthur kinetics is unable to form Turing structure [30], whereas the same system in the presence of taxis can show stationary Turing patterns [40, 42]. We extend the temporal model (3) to include random movement due to diffusion and directed movement of the predator population because of prey-taxis. Thus, our spatio-temporal model becomes

$$\frac{\partial N}{\partial T} = D_1 \nabla^2 N + N(\sigma - \eta N) - \frac{\alpha NP}{1 + \beta N^2}, \quad X \in \tilde{\Omega}, \quad T > 0, \quad (4a)$$

$$\frac{\partial P}{\partial T} = D_2 \nabla^2 P + \nabla \cdot (\chi(N)P \nabla N) + \frac{\zeta \alpha NP}{1 + \beta N^2} - \gamma P - \delta P^2, \quad X \in \tilde{\Omega}, \quad T > 0, \quad (4b)$$

where $\tilde{\Omega} \subset \mathbb{R}^n$ is a bounded domain with boundary $\partial \tilde{\Omega}$. Further, D_1 and D_2 respectively are the self-diffusion coefficients of the prey and predator species, and χ is the prey-taxis coefficient. Note that $\chi < 0$ and $\chi > 0$ corresponds to attractant and repellent prey-taxis respectively [43, 44]. Due to group defense by the prey species, the predator species prefer low-density prey areas for their hunting and avoid high-density prey areas. Our temporal model incorporates the group defense in prey species through a non-monotonic functional response. To take into account the group defense induced prey-taxis in the RD model, we take $\chi(N) = \chi_0 > 0$, where χ_0 is a constant for simplicity [35, 44, 45]. A dimensionless version of (4), using $u = \frac{\eta}{\sigma} N$, $v = \frac{\delta}{\sigma} P$, $t = \sigma T$ and $x = \sqrt{\frac{\sigma}{D_1}} X$ for dimensionless prey, predator, time and space, is

$$\frac{\partial u}{\partial t} = \nabla^2 u + u(1 - u) - \frac{auv}{1 + bu^2}, \quad x \in \Omega, \quad t > 0 \quad (5a)$$

$$\frac{\partial v}{\partial t} = d \nabla^2 v + c \nabla \cdot (v \nabla u) + \frac{eauv}{1 + bu^2} - fv - v^2, \quad x \in \Omega, \quad t > 0, \quad (5b)$$

where $a = \frac{\alpha}{\delta}$, $b = \frac{\beta\sigma^2}{\eta^2}$, $c = \frac{\chi\sigma}{D_1\eta}$, $d = \frac{D_2}{D_1}$, $e = \frac{\zeta\delta}{\eta}$ and $f = \frac{\gamma}{\sigma}$, are dimensionless positive parameters. Here, Ω is the dimensionless domain with corresponding boundary $\partial\Omega$, and d is the ratio of self-diffusion of predator and prey. Further, $c > 0$ represents the dimensionless prey-taxis coefficient that characterizes the tendency of the predator population to keep away from the high-density prey areas. The system (5) is subjected to non-negative initial conditions $u(x, 0) \equiv u_0(x)$ and $v(x, 0) \equiv v_0(x)$ for $x \in \Omega$, and no-flux boundary conditions $\frac{\partial u}{\partial n} = \frac{\partial v}{\partial n} = 0$ for $x \in \partial\Omega$ and $t > 0$.

Long transient dynamics is currently an important topic for predicting and managing ecological systems in the face of environmental change [46]. It refers to the slowly varying dynamics over a long period of time before the system reaches its final state. This long transient dynamics can be complex and unpredictable, which may appear as stationary, oscillatory or even chaotic [46, 47, 48]. In the context of dynamical system, these transient dynamics are guided by various temporal and spatio-temporal bifurcations. The length of this transient period depends on the distance of the control parameter from the bifurcation threshold and initial conditions [46, 49]. Here, we show interesting long transient dynamics for the temporal and spatio-temporal system, which are unpredictable in their final state.

The predator species do not have any cooperative nature due to the Bazykin-type reaction kinetics in contrast to prey species for which group defense is a kind of cooperative behavior [9, 10, 11]. To the best of our knowledge, this is the first study to investigate group defense-induced prey-taxis in an ecological model. For the temporal model, we perform a bifurcation analysis and illustrate some representative dynamics through one- and two-parametric bifurcation diagrams. We establish global existence and boundedness of solutions for the spatio-temporal model with Neumann boundary conditions. The stability of the homogeneous steady states and Turing instability are discussed for the spatio-temporal model. The existence of a non-homogeneous stationary solution is shown using weakly nonlinear analysis (WNA) which is then validated with numerical solution. A key strength of our work is the investigation of long transient dynamics. We have established the roles of local and global bifurcations on the stationary and oscillatory transient dynamics exhibited by the temporal model. The fate of these transient dynamics under the influence of diffusion and taxis have also been investigated. For certain parameter values, appearance of steady homogeneous solution in Turing domain and non-homogeneous in space but oscillatory in time solution in Hopf domain are some other key findings of our work.

The temporal model together with its equilibria, stability, local and global bifurcations are described in Section 2. This section also contains long transient dynamics with numerical visualization. Section 3 consists of the global existence and boundedness of the spatio-temporal solution, stability analysis of the homogeneous steady states, and Turing bifurcation. The derivation of the amplitude equation using WNA has been carried out in Section 4. Using numerical simulations, we validate the results of WNA in Section 5. This section also contains an extensive range of numerical simulations that show long transient dynamics as well as various interesting stationary and dynamic patterns. Finally, the paper concludes with a comprehensive discussion in Section 6.

2 Temporal model

Here, we discuss temporal dynamics corresponding to the homogeneous system of (5), i.e.,

$$\frac{du}{dt} = u(1 - u) - \frac{auv}{1 + bu^2} \equiv F_1(u, v) \equiv uf_1(u, v), \quad (6a)$$

$$\frac{dv}{dt} = \frac{eauv}{1 + bu^2} - fv - v^2 \equiv F_2(u, v) \equiv vf_2(u, v). \quad (6b)$$

The system (6) is subjected to non-negative initial conditions $u(0) \geq 0, v(0) \geq 0$.

2.1 Positivity and boundedness

Theorem 1. *Every solution $(u(t), v(t))$ of the system (6) with non-negative initial condition remains bounded and non-negative for all time t .*

Proof. The proof is straightforward and has been omitted. □

2.2 Existence and stability of equilibria

Here, we discuss the number and types of all possible equilibria in $\mathbb{R}_2^+ = \{(u, v) : u \geq 0, v \geq 0\}$. The system (6) has trivial equilibrium point $E_0(0, 0)$ and axial equilibrium point $E_1(1, 0)$ irrespective of parameter values.

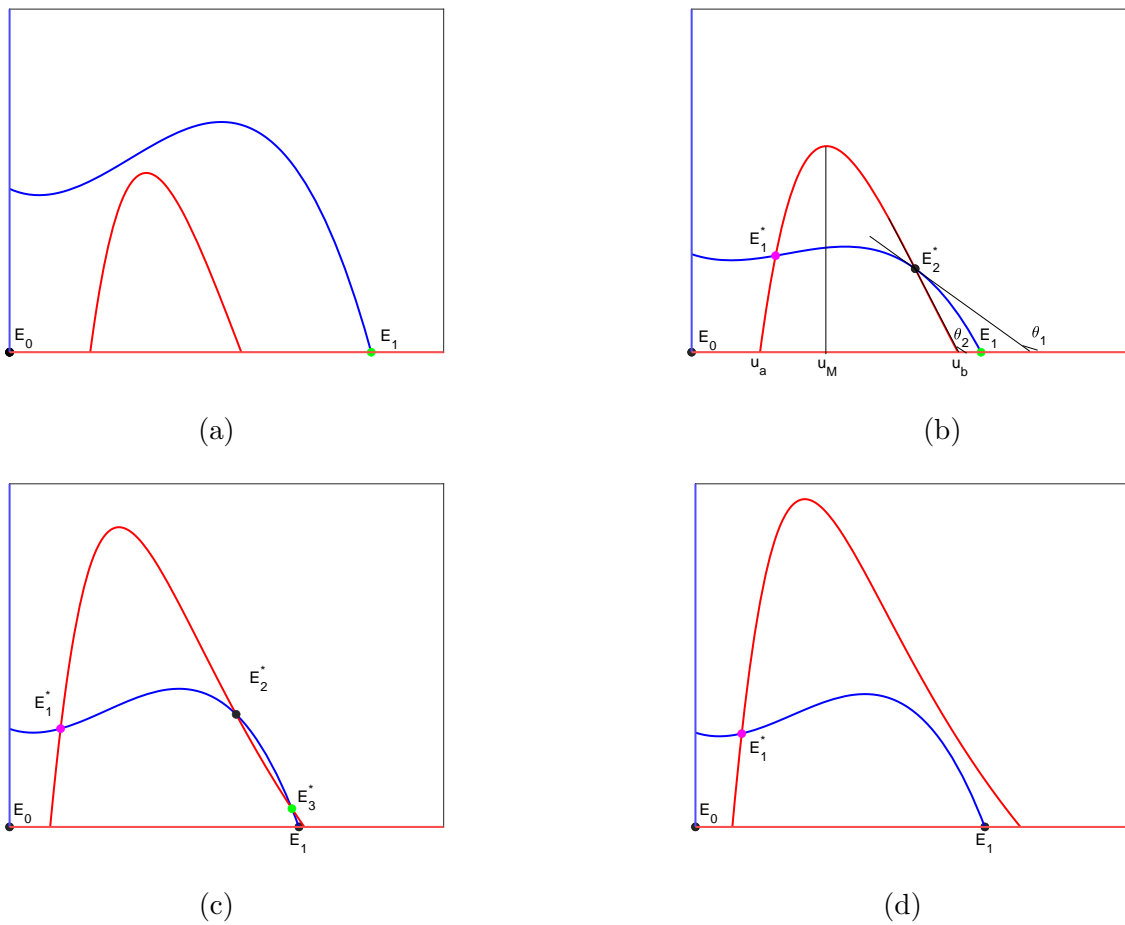


Figure 1: Location of nullclines and equilibria of the system (6) for all possible cases. Here blue and red color curves denote the prey and predator nullclines respectively and dots represent various equilibria. Green and black dots represent the stable and saddle equilibria respectively and the stability of magenta dots depends on the Hopf bifurcation.

An interior equilibrium $E_j^*(u_j^*, v_j^*)$ (where j can be 1, 2 or 3) is a point of intersection of the non-trivial prey nullcline $v = n(u) := \frac{(1 + bu^2)(1 - u)}{a}$ and predator nullcline $v = p(u) := \frac{eau}{bu^2 + 1} - f$.

The prey component u_j^* of the interior equilibrium E_j^* satisfies

$$Q(u) \equiv b^2 u^5 - b^2 u^4 + 2bu^3 - b(af + 2)u^2 + (a^2 e + 1)u - (af + 1) = 0, \quad (7)$$

and the component v_j^* is obtained from

$$v_j^* = \frac{eau_j^*}{bu_j^{*2} + 1} - f.$$

Now, $n(u) \geq 0$ for $u \leq 1$ and $p(u)$ intersects u axis at two points, say $(u_a, 0)$ and $(u_b, 0)$, where

$$u_a = \frac{ea - \sqrt{e^2 a^2 - 4bf^2}}{2bf} \quad \text{and} \quad u_b = \frac{ea + \sqrt{e^2 a^2 - 4bf^2}}{2bf}, \quad \text{whenever } e^2 a^2 \geq 4bf^2.$$

Thus, we must have $u_a < u^* < \min\{1, u_b\}$ for feasibility of E^* . Also, $p(u)$ has a maximum at $u_M = \frac{1}{\sqrt{b}}$. The system (6) has at least one coexisting equilibrium point when $p(u_M) \geq n(u_M)$. In

the case of two equilibria, we label them as $E_1^*(u_1^*, v_1^*)$ and $E_2^*(u_2^*, v_2^*)$ with $0 < u_1^* < \frac{1}{\sqrt{b}} < u_2^* < 1$ [see Fig. 1(b)]. The system can have three equilibria for parameter value $f_{SN_2} < f < f_{TC}$ with $0 < u_1^* < \frac{1}{\sqrt{b}} < u_2^* < u_{sn_1} < u_3^* < 1$, where u_{sn_1} and f_{SN_2} are discussed in the next subsection. Depending on the parameter restriction, we summarize the number of equilibria in Table 1. Next, we discuss the stability of the different equilibria. The Jacobian of the system (6) at a point $E(u, v)$ is given by

$$J(E) = \begin{bmatrix} 1 - 2u + \frac{av(bu^2 - 1)}{(bu^2 + 1)^2} & -\frac{au}{bu^2 + 1} \\ \frac{eav(1 - bu^2)}{(bu^2 + 1)^2} & \frac{eau}{bu^2 + 1} - f - 2v \end{bmatrix} \equiv \begin{bmatrix} a_{10} & a_{01} \\ b_{10} & b_{01} \end{bmatrix}. \quad (8)$$

Considering the Jacobian matrix (8) at an equilibrium point, we have the following propositions:

Proposition 1. *The trivial equilibrium point E_0 is always a saddle point and the axial equilibrium point E_1 is a saddle point for $f < f_{TC} := \frac{ea}{b+1}$ and asymptotically stable for $f > f_{TC}$.*

Proof. Since, the eigenvalues of $J(E_0)$ are 1 and $-f$, it is always a saddle point. The eigenvalues of $J(E_1)$ are -1 and $\frac{ea}{b+1} - f$. Therefore, E_1 is asymptotically stable when $f > f_{TC}$ and a saddle point when $f < f_{TC}$. \square

Proposition 2. *For $p(u_M) \geq n(u_M)$ and $e^2 a^2 \geq 4bf^2$, the system (6) has at least one coexisting equilibrium and at most three different coexisting equilibria. The following hold for the stability of the co-existing equilibria:*

- (i) E_1^* is asymptotically stable for $b < b_H$ and unstable for $b > b_H$, where b_H is defined in the text.
- (ii) Whenever E_2^* exists, it is always a saddle point.
- (iii) Whenever E_3^* exists, it is always asymptotically stable.

Proof. The Jacobian $J(E^*)$, at a coexisting equilibrium point $E^*(u^*, v^*)$, is given by

$$J(E^*) = \begin{bmatrix} u \frac{\partial f_1}{\partial u} & u \frac{\partial f_1}{\partial v} \\ v \frac{\partial f_2}{\partial u} & v \frac{\partial f_2}{\partial v} \end{bmatrix}_{(u^*, v^*)} = \begin{bmatrix} -u \frac{\partial f_1}{\partial v} \frac{dv}{du}(f_1) & u \frac{\partial f_1}{\partial v} \\ -v \frac{\partial f_2}{\partial v} \frac{dv}{du}(f_2) & v \frac{\partial f_2}{\partial v} \end{bmatrix}_{(u^*, v^*)},$$

Table 1: Existence and stability of different equilibria of the system (6).

Equilibria	Existence criteria	Stability criteria
E_0	independent of parameter values	saddle point.
E_1	independent of parameter values	a saddle point if $f < f_{TC}$, and asymptotically stable if $f > f_{TC}$.
E_1^*	$p(u_M) \geq n(u_M)$ and $e^2 a^2 \geq 4bf^2$	asymptotically stable if $b < b_H$, and unstable if $b > b_H$.
E_2^*	$p(u_M) > n(u_M)$, $e^2 a^2 \geq 4bf^2$ with either $u_b < 1$ or $u_b > 1$ and $f_{SN_2} < f < f_{TC}$	saddle point.
E_3^*	$p(u_M) > n(u_M)$, $e^2 a^2 \geq 4bf^2$, $u_b > 1$ and $f_{SN_2} < f < f_{TC}$	asymptotically stable.

where $\frac{dv}{du}^{(f_j)}$ represents the slope of the tangent to the curve $f_j(u, v) = 0$ ($j = 1, 2$). Also,

$$\det(J(E^*)) = \left(uv \frac{\partial f_1}{\partial v} \frac{\partial f_2}{\partial v} \left(\frac{dv}{du}^{(f_2)} - \frac{dv}{du}^{(f_1)} \right) \right)_{(u^*, v^*)}. \quad (9)$$

We observe that

$$\frac{\partial f_1(u^*, v^*)}{\partial v} = -\frac{a}{1 + bu^2} < 0 \quad \text{and} \quad \frac{\partial f_2(u^*, v^*)}{\partial v} = -1.$$

Suppose that θ_1 and θ_2 respectively denote the inclination angles of the tangents to $f_1(u, v) = 0$ and $f_2(u, v) = 0$ at E_2^* [see Fig. 1(b)]. We find that $\frac{\pi}{2} < \theta_2 < \theta_1 < \pi$ holds whenever E_2^* exists, which implies

$$\left. \frac{dv}{du}^{(f_2)} \right|_{(u_2^*, v_2^*)} < \left. \frac{dv}{du}^{(f_1)} \right|_{(u_2^*, v_2^*)}.$$

Hence, we have $\det(J(E_2^*)) < 0$ from (9) and therefore E_2^* is a saddle point. Similarly, we obtain $\det(J(E_1^*)) > 0$ for E_1^* . Using Routh-Hurwitz stability criteria, the coexisting equilibrium point E_1^* is asymptotically stable if $\text{tr}(J(E_1^*)) < 0$, which holds when

$$b < b_H := \frac{u_1^* + v_1^*}{u_1^{*2} (2 - 3u_1^* - v_1^*)}.$$

Thus, E_1^* is asymptotically stable for $b < b_H$ and unstable for $b > b_H$.

The coexisting equilibrium point E_3^* exchanges stability with stable E_1 through a transcritical bifurcation at $f = f_{TC}$ (discussed in the next subsection) and it is feasible for $f < f_{TC}$. Therefore, it is asymptotically stable whenever it exists. \square

2.3 Local bifurcation Analysis

Here, we discuss transcritical, saddle-node, Hopf, generalized Hopf (GH), and Bautin bifurcations exhibited by the system (6).

2.3.1 Transcritical bifurcation

Proposition 3. *The temporal model (6) encounters a transcritical bifurcation at E_1 when the parameter f satisfies the threshold $f = f_{TC} = \frac{ea}{b+1}$.*

Proof. The Jacobian matrix $J(E_1)$ given in (8) has a zero eigenvalue at $f = f_{TC}$. Let the eigenvectors of the Jacobian matrix $J(E_1)$ and its transpose $J(E_1)^T$ corresponding to the zero eigenvalue be $\zeta = [\frac{a}{b+1}, 1]^T$ and $\eta = [1, 0]^T$ respectively. Now, the transversality conditions [50] become

$$\begin{aligned}\eta^T \mathcal{F}_f(E_1; f = f_{TC}) &= 0, \\ \eta^T D\mathcal{F}_f(E_1; f = f_{TC})\zeta &= 0, \\ \eta^T D^2\mathcal{F}(E_1; f = f_{TC})(\zeta, \zeta) &= -4 \frac{a^2}{(b+1)^3} \neq 0.\end{aligned}$$

Here, $\mathcal{F} = [F_1(u, v), F_2(u, v)]^T$ and all the other notations are the same as in [50]. Thus, all the transversality conditions of degenerate transcritical bifurcation [51, 52] are satisfied for the system (6) when $f = f_{TC}$. \square

2.3.2 Saddle-node bifurcation

Suppose that for the polynomial Q given in (7), there exist two real roots, say u_{sn_1} and u_{sn_2} of $Q'(u) = 0$ with $0 < u_{sn_1} < u_{sn_2}$. Then, opposite signs of $Q(u_{sn_1})$ and $Q(u_{sn_2})$ lead to three positive roots u of the equation $Q(u) = 0$ with $u_1^* < u_{sn_1} < u_2^* < u_{sn_2} < u_3^*$ [see Fig. 2(a)]. Note that for the feasibility of coexisting equilibria, we must have $u_i^* < \min\{1, u_b\}$ for $i = 1, 2, 3$. A variation in one temporal parameter may result in two cases: either E_2^* coincides with E_1^* when $Q(u_{sn_1}) = 0$ [see Fig. 2(b)] or E_2^* coincides with E_3^* when $Q(u_{sn_2}) = 0$ [see Fig. 2(c)] provided $u_{sn_i} < \min\{1, u_b\}$ for $i = 1, 2$. Thus, a saddle-node bifurcation SN_1 occurs in the former case and another saddle-node bifurcation SN_2 occurs in the latter case. Taking f as the control parameter, the threshold value for SN_1 is given by

$$f_{SN_1} = \frac{5b^2u_{sn_1}^4 - 4b^2u_{sn_1}^3 + 6bu_{sn_1}^2 - 4bu_{sn_1} + a^2e + 1}{2ab}.$$

To obtain the threshold value f_{SN_2} , we replace u_{sn_1} with u_{sn_2} in the expression for f_{SN_1} . In the following proposition, transversality conditions are verified for this bifurcation.

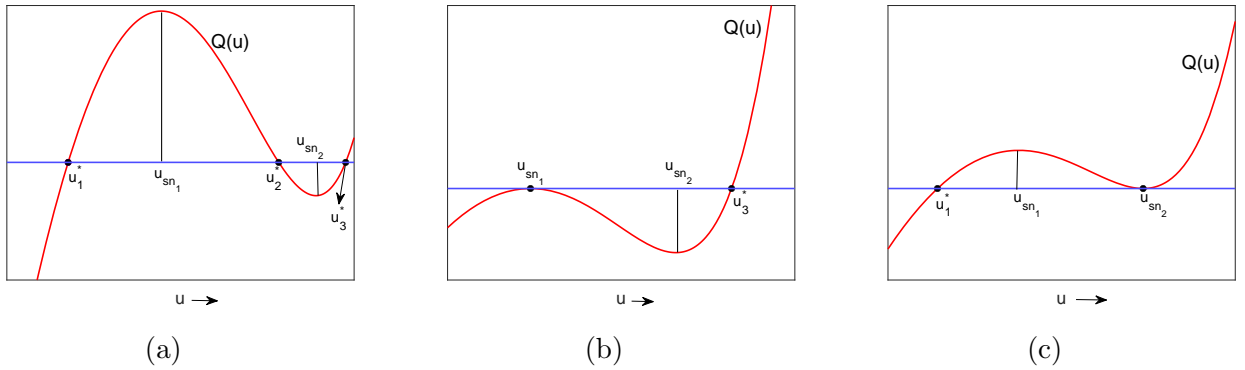


Figure 2: Plot of $Q(u)$ for three different cases.

Proposition 4. *When $Q(u) = 0$ has a double root $u < \min\{1, u_b\}$, then the temporal system (6) exhibits saddle-node bifurcation when the control parameter f is varied.*

Proof. Suppose that u_{sn} , with $u_{sn} < \min\{1, u_b\}$, is a double root of $Q(u) = 0$, i.e., $Q(u_{sn}) = Q'(u_{sn}) = 0$ but $Q''(u_{sn}) \neq 0$ when $f = f_{SN}$. Let the corresponding interior equilibrium point be

$E_{SN}^* = (u_{sn}, v_{sn})$. Therefore, the nontrivial nullclines $f_1(u, v) = 0$ and $f_2(u, v) = 0$ touch each other at E_{SN}^* , where both of them have same slope $\frac{dv^{(f_1)}}{du}|_{E_{SN}^*} = \frac{dv^{(f_2)}}{du}|_{E_{SN}^*}$. Using $\frac{dv^{(g)}}{du} = -\frac{\frac{\partial g}{\partial u}}{\frac{\partial g}{\partial v}}$, we find

$$\det(J(E_{SN}^*)) = \left[uv \left(\frac{\partial f_1}{\partial u} \frac{\partial f_2}{\partial v} - \frac{\partial f_1}{\partial v} \frac{\partial f_2}{\partial u} \right) \right]_{E_{SN}^*} = 0.$$

Therefore, the Jacobian matrix $J(E_{SN}^*)$ has a zero eigenvalue. Let $\zeta = [p, 1]^T$ and $\eta = [1, q]^T$ respectively be the eigenvectors of $J(E_{SN}^*)$ and $[J(E_{SN}^*)]^T$ corresponding to the zero eigenvalue, where

$$p = -\frac{a}{1 + (3u_{sn}^2 - 2u_{sn})b} \quad \text{and} \quad q = -\frac{au}{(bu^2 + 1)v}.$$

To check the transversality conditions, we calculate

$$\eta^T \mathcal{F}_f(E_{SN}^*; f = f_{SN}) = \frac{au_{sn}}{bu_{sn}^2 + 1},$$

$$\eta^T D^2 \mathcal{F}(E_{SN}^*; f = f_{SN})(\zeta, \zeta) = \left(\frac{\partial^2 F_1}{\partial u^2} p^2 + 2 \frac{\partial^2 F_1}{\partial u \partial v} p + \frac{\partial^2 F_1}{\partial v^2} + q \left(\frac{\partial^2 F_2}{\partial u^2} p^2 + 2 \frac{\partial^2 F_2}{\partial u \partial v} p + \frac{\partial^2 F_2}{\partial v^2} \right) \right)_{(E_{SN}^*; f_{SN})},$$

where we omit explicit expressions in the last equation since it is too cumbersome. The system (6) undergoes a non-degenerate saddle-node bifurcation [50] at $f = f_{SN}$ if $\eta^T \mathcal{F}_f(E_{SN}^*; f = f_{SN}) \neq 0$ and $\eta^T D^2 \mathcal{F}(E_{SN}^*; f = f_{SN})(\zeta, \zeta) \neq 0$. Clearly, the first conditions is satisfied and the last condition is verified numerically. \square

2.3.3 Cusp bifurcation

We have found that a transcritical bifurcation TC occurs at E_1 and a saddle-node bifurcation SN_2 occurs at $E_{SN_2}^* = (u_{sn_2}, v_{sn_2})$ with variation of the control parameter f . Now, $E_{SN_2}^*$ and E_1 coincide with the variation of a different temporal parameter b . Thus, the saddle-node bifurcation curve SN_2 and transcritical curve TC intersect at a cusp bifurcation point (f_{CP}, b_{CP}) in the f - b parametric plane.

Proposition 5. *The system (6) encounters a cusp bifurcation when $Q(1) = Q'(1) = 0$.*

Proof. Suppose at $f = f_{CP}$ and $b = b_{CP}$, interior equilibria E_2^* and E_3^* coincide with the axial equilibrium point E_1 . Here, the curves TC and SN_2 , corresponding to the transcritical and saddle-node bifurcations respectively, meet at the cusp bifurcation point (f_{CP}, b_{CP}) in the f - b plane. From proposition 4, we know that $Q(u)$ has a double root. Since transcritical bifurcation also happens simultaneously, $Q(u)$ has a double root 1, i.e., $Q(1) = Q'(1) = 0$ at the cusp bifurcation threshold. Here, f_{CP} is the positive root of the equation $2z^3 - ae z^2 + ae^2 = 0$ and the corresponding $b_{CP} = (ae - f_{CP})/f_{CP}$. \square

2.3.4 Hopf and Bautin bifurcation

At a Hopf-bifurcation threshold, a stable equilibrium point changes stability and a limit cycle is generated that can be stable or unstable. In proposition 2(i), we have observed that the interior equilibrium E_1^* changes its stability when the trace of $J(E_1^*)$ changes its sign due to variation in b . We thus have $tr(J(E_1^*)) = 0$ at the Hopf bifurcation threshold $b = b_H$. Since (u_1^*, v_1^*) depends on b ,

the threshold b_H is an implicit expression. The temporal system (6) exhibits a Hopf bifurcation at $b = b_H$ if the non-hyperbolicity and transversality conditions given below are satisfied:

$$\begin{aligned} H1 : \quad & \det[J(E_1^*; b = b_H)] > 0, \\ H2 : \quad & \frac{d}{db}(\text{tr}[J(E_1^*)])|_{b=b_H} \neq 0. \end{aligned}$$

Hopf-bifurcations are classified as supercritical or subcritical depending on the stability of the generated limit cycle. Supercritical Hopf-bifurcation occurs when the limit cycle is stable, whereas subcritical Hopf-bifurcation occurs when the limit cycle is unstable. The first case corresponds to the first Lyapunov coefficient $l_1 < 0$, whereas the second one corresponds to $l_1 > 0$ [50]. Due to the unavailability of explicit expression of interior equilibrium E_1^* , it is difficult to determine the sign of l_1 analytically. However, we obtain the value of l_1 numerically using the Matcont software. If we fix the temporal parameters $a = 7$, $f = 1.05$ and $e = 0.95$, then the system (6) exhibits a subcritical Hopf bifurcation around $E_1^* = (0.2412, 0.1455)$ at $b_H = 5.8759$ with $l_1 = 0.0085$. For the same parameter values except $f = 1.06$, a supercritical Hopf bifurcation has been found around $E_1^* = (0.2443, 0.1455)$ at $b_H = 5.8234$ with $l_1 = -0.043$.

Clearly, the first Lyapunov coefficient l_1 vanishes between $f = 1.05$ and $f = 1.06$ with $a = 7$ and $e = 0.95$. When l_1 becomes zero, the system (6) undergoes a codimension-2 bifurcation known as a Bautin bifurcation or generalized Hopf bifurcation (GH). A global saddle-node bifurcation curve of the limit cycle, where a stable limit cycle collides with an unstable limit cycle, emerges from the GH point in the two-parametric plane of bifurcation. The system (6) undergoes Bautin bifurcation at $E_1^* = (0.2417, 0.1455)$ for the bifurcating parameter values $f_{GH} = 1.0517$ and $b_{GH} = 5.8671$ with $a = 7$ and $e = 0.95$.

2.3.5 Bogdanov-Takens bifurcation

A Bogdanov-Takens (BT) bifurcation is a codimension-2 bifurcation that occurs in a dynamical system when a Hopf bifurcation collides with a saddle-node bifurcation. The system (6) exhibits a Hopf bifurcation and two saddle-node bifurcations which suggests that a BT bifurcation may occur in our system. Both the determinant and trace of the Jacobian matrix, evaluated at an equilibrium point, vanish simultaneously at a BT bifurcation point. A homoclinic or heteroclinic global bifurcation curve comes out from the BT point in the two-parametric bifurcation plane. Here, we take f and b as control parameters for BT bifurcation. For fixed parameter values $a = 7$ and $e = 0.95$, the system (6) exhibits a BT bifurcation for $E_1^*(0.4086, 0.1637)$ at $(f_{BT}, b_{BT}) = (1.2388, 5.6146)$.

2.4 Numerical visualisation

Here, we visualize previously described local and global bifurcations with the help of numerical simulations. For fix parameter values $a = 7$, $e = 0.95$, we plot a two-dimensional bifurcation diagram in the f - b parametric plane (see Fig. 3). The coordinate of the cusp point (CP) is (1.2270, 4.4195) and the coordinates of GH and BT points have already been mentioned earlier.

To better understand how the system dynamics change across the local and global bifurcation curves in Fig. 3, we consider four different values of b and plot their corresponding one-parametric bifurcation diagrams in Fig. 4. For $b = 4.2$, equilibria E_1^* and E_2^* appear in the system through the saddle-node bifurcation SN_1 , and E_2^* disappears from feasibility region through a transcritical bifurcation TC [see Fig. 4(a)]. For $b = 5.2$, two qualitative changes are observed [see Fig. 4(b)]. First, the system (6) exhibits another saddle-node bifurcation SN_2 . Second, two supercritical Hopf bifurcations occur around E_1^* which leads to an oscillatory coexisting solution between two Hopf

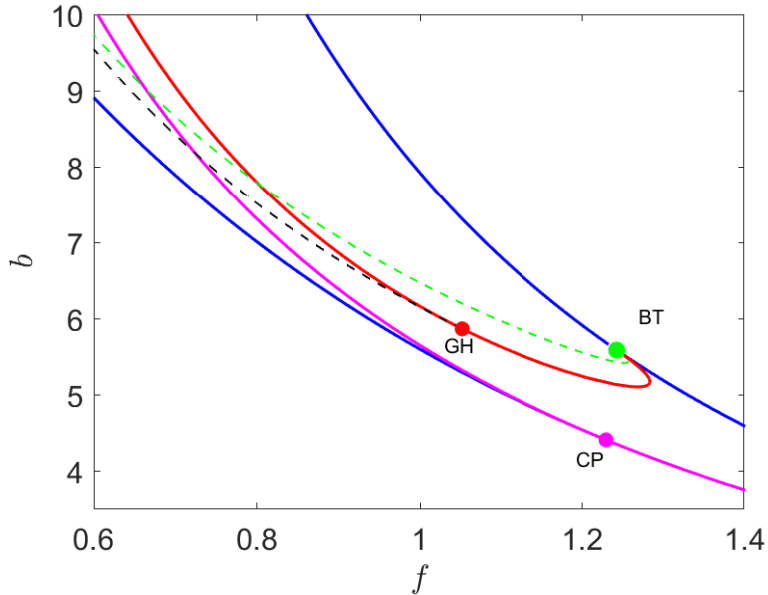


Figure 3: Two parametric bifurcation diagram in the f - b plane. Magenta, blue, and red colour curves represent the transcritical, saddle-node, and Hopf bifurcations respectively. Here, the upper and lower blue curves represent the SN_1 and SN_2 , respectively. The green and black dashed curves denote the global curves, namely homoclinic and saddle-node bifurcation of limit cycles, respectively. Further, colored solid dots represent codimension-2 bifurcation points. Other parameter values are $a = 7$ and $e = 0.95$.

bifurcation thresholds. Note that these two Hopf bifurcation points lie on the same Hopf curve (marked by red color) below the BT point in Fig. 3. The system (6) shows a bistable dynamics in between E_1^* and E_3^* for parameter value in $f_{SN_2} < f < f_{TC}$.

Figures 4(a) and (b) correspond to parameter value $b < b_{BT}$. Now, we consider the case $b > b_{BT}$ for which two bifurcation diagrams are shown in Figs. 4(c) and (d). Here, the coexisting equilibrium point E_1^* , generated due to saddle-node bifurcation SN_1 , becomes unstable compared to the stable case for $b < b_{BT}$. The Hopf bifurcating limit cycle disappears due to collision with the coexisting equilibria E_2^* through a homoclinic bifurcation for $b_{BT} < b < b_{GH}$ [see Fig. 4(c)]. For $b > b_{GH}$, the Hopf bifurcation becomes subcritical and the corresponding bifurcation diagram is shown in Fig. 4(d). A stable and an unstable limit cycles are generated due to a global homoclinic bifurcation (HOM) and a subcritical Hopf bifurcation respectively. These two limit cycles collide and disappear from the system dynamics through the saddle-node bifurcation of limit cycles (SNLC). Interestingly, the system shows tristability among three attractors, specifically, two equilibria E_1^* , E_1 and the stable limit cycle around E_1^* for parameter value $f_{SNLC} < f < f_H$. The unstable limit cycle around E_1^* and the stable manifold of the E_2^* act as separatrix of these three attractors.

Temporal transient dynamics

Here we explore some interesting long-temporal transient dynamics of the system (6) due to the global and local bifurcations. We consider the same parameter values as in Fig 4(d) and f is chosen near the SN_2 threshold $f_{SN_2} = 0.801336$. A long transient dynamics is observed in the time evolution of u for values of f near f_{SN_2} starting from same initial condition $(u(0), v(0)) \equiv (1.4, 0.05)$. To investigate this in detail, we consider the time evolution of u for three different values of f near f_{SN_2} [see Fig. 5(a)]. For $f = 0.802$, the equilibrium point E_3^* is asymptotically stable and the

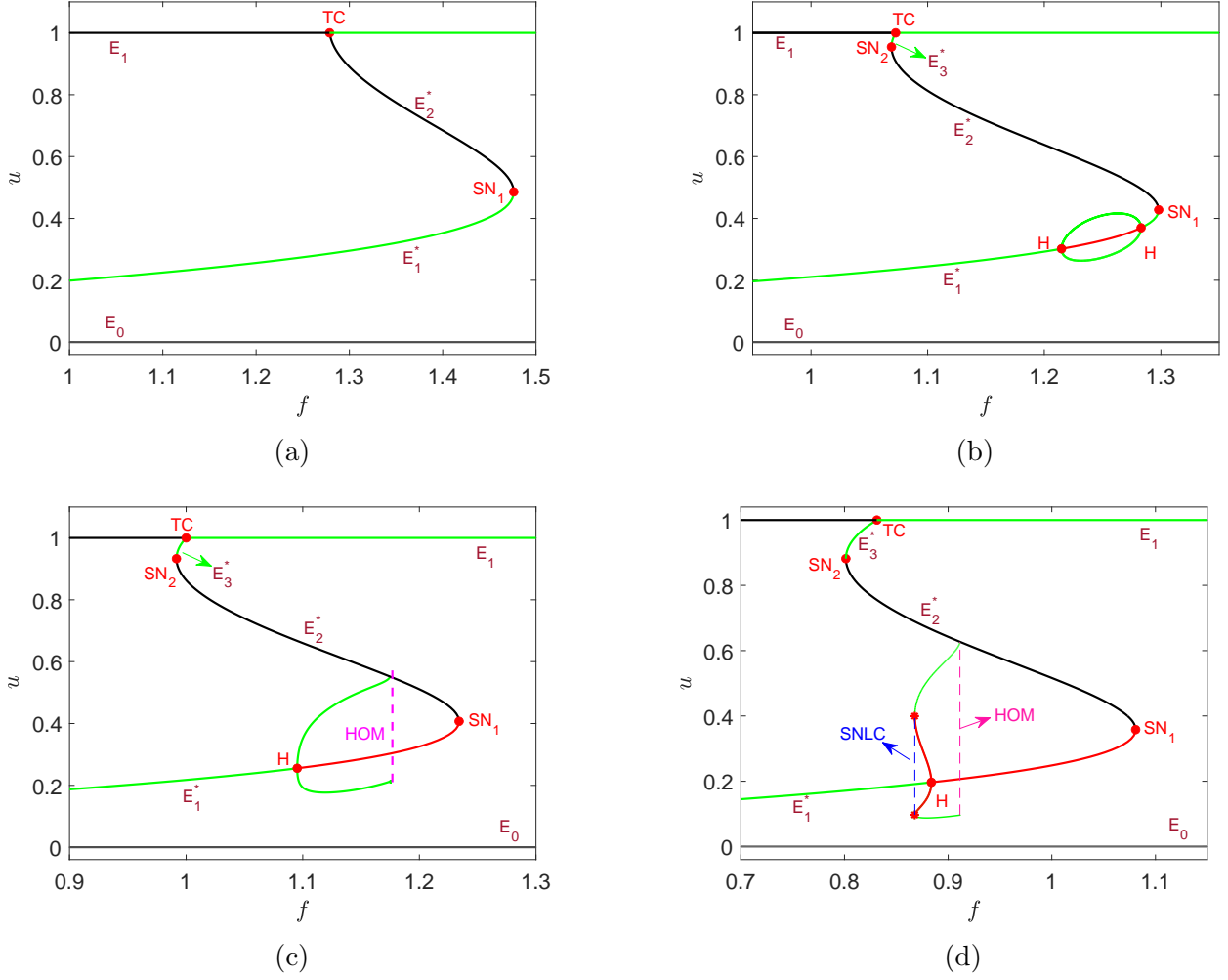


Figure 4: Bifurcation diagram of the system (6) against parameter f for different values of b : (a) $b = 4.2$, (b) $b = 5.2$, (c) $b = 5.65$, and (d) $b = 7$. Here SN_1 and SN_2 represent saddle-node bifurcations; TC and H denote transcritical and Hopf bifurcations respectively. Also, SNLC and HOM represent the saddle-node bifurcation of limit cycles and homoclinic bifurcation respectively. Other parameter values are $a = 7$ and $e = 0.95$.

time evolution of u approaches E_3^* rapidly. Note that E_3^* disappears for $f < f_{SN_2} = 0.801336$ due to a saddle-node bifurcation. The time evolution of u also rapidly approaches the globally stable equilibrium point E_1^* for $f = 0.80$. However, if we take $f = 0.8013$, then u spends a considerable amount of time near the solution for $f = 0.802$. However, equilibrium point E_3^* is not present in the system for $f = 0.8013$ and the time evolution of u finally settles into the globally stable equilibrium state E_1^* . Here, a shadow of E_3^* acts as a ghost attractor in the system (6) which causes such long transient dynamics. This long transient dynamics is also observed for other initial conditions too. Time evolution of u shows similar behaviour for $f = 0.8013$ if the initial condition lies in the shaded region shown in Fig. 5(b). When a trajectory passes through the narrow region between the nullclines [see the inset of the Fig. 5(b)], their u directional as well as v directional velocities become very small. This leads to the phenomenon of ghost attractor and long transient dynamics in the system. Figure 5(a) also illustrates hysteresis exhibited by the system (6). A small change in the parameter f results in a significant drop or change (from E_3^* to E_1^*) in the steady state solution.

The system (6) also exhibits oscillatory long transient dynamics due to the global SNLC bi-

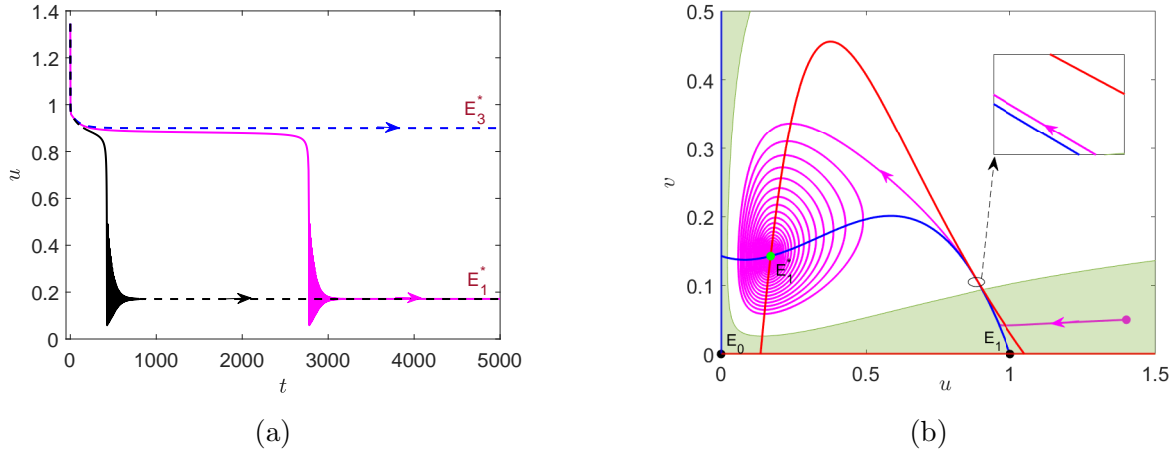


Figure 5: Temporal transient dynamics due to saddle-node bifurcation for $a = 7$, $b = 7$ and $e = 0.95$ with $(u(0), v(0)) = (1.4, 0.05)$ as initial condition. (a) Here, blue, magenta, and black colour curves correspond to time evolution of u for $f = 0.802$, $f = 0.8013$, and $f = 0.80$ respectively. (b) Phase trajectory for $f = 0.8013$ marked with magenta colour curve. The prey and predator nullclines are also shown. Any solution starting with the initial condition in the shaded region exhibits long transient dynamics similar to that of $f = 0.8013$.

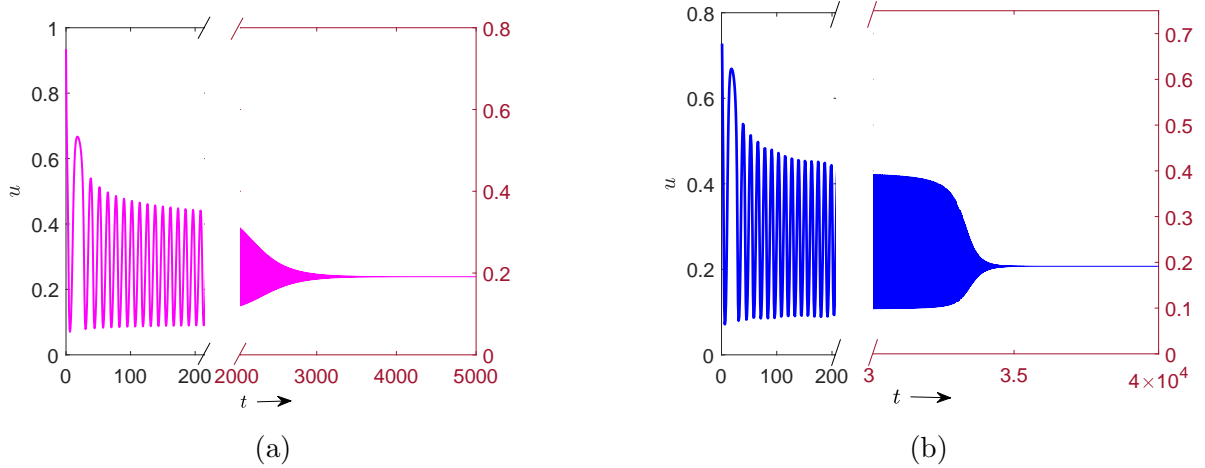


Figure 6: Time evolution of u showing long oscillatory transient dynamics due to global bifurcation SNLC with $(u(0), v(0)) = (0.97, 0.45)$ as initial condition: (a) $f = 0.867$ and (b) $f = 0.867682$. Other parameter values are $a = 7$, $b = 7$, and $e = 0.95$.

furcation. The coexisting equilibrium point E_1^* is surrounded by an unstable limit cycle, that is also surrounded by a stable limit cycle for $f_{SNLC} = 0.867805 < f < f_H = 0.883805$. Both the limit cycles collide and disappear from the system dynamics through the SNLC. We have plotted the time evolution of u for two different values of f near f_{SNLC} in Fig. 6 with initial condition $(u(0), v(0)) = (0.97, 0.45)$. The coexisting equilibrium point E_1^* is locally asymptotically stable for $f < f_{SNLC}$. The time evolution of u converges to E_1^* faster for $f = 0.867$ compared to that for $f = 0.867682$. Thus, oscillatory long transient dynamics is observed for values of f near f_{SNLC} due to global SNLC bifurcation.

3 Spatio-temporal model

Now, we consider the spatio-temporal model (5) to examine the effects of taxis and diffusion on the dynamics. We first establish global existence and boundness of the solution using L^p - L^q estimates. Next, we examine the stability of the homogeneous steady states by converting the spatio-temporal problem to an eigenvalue problem. Finally, the Turing bifurcation threshold is also obtained.

3.1 Global existence and boundedness of solution

The global existence and boundedness of solution with different taxis and reaction kinetics have been established in [53, 54, 55]. Here, we establish the same with non-monotonic functional response. Let $W^{1,p}(\Omega)$ be the Sobolev space consisting of functions in $L^p(\Omega)$ that have weak first order partial derivatives and they belong to $L^p(\Omega)$.

Lemma 1. *Assume that $(u_0, v_0) \in [W^{1,p}(\Omega)]^2$ with $u_0, v_0 \geq 0$ and $p > n$. Then the following hold for the system (5)*

(i) *There exists a positive constant T (maximal existence time) such that the system (5) has a unique local-in-time non-negative solution $(u(x, t), v(x, t)) \in [C(\bar{\Omega} \times [0, T]) \cap C^{2,1}(\bar{\Omega} \times (0, T))]^2$.*

(ii) *The L_1 bounds of $(u(x, t), v(x, t))$, for all time $t \in (0, T)$, satisfy*

$$\int_{\Omega} u(x, t) dx \leq A \text{ and } \int_{\Omega} v(x, t) dx \leq B,$$

where A and B are defined in the proof.

(iii) *There exists a constant C such that $0 \leq u(x, t) \leq C$ and $v(x, t) \geq 0$ for all $(x, t) \in \bar{\Omega} \times (0, T)$.*

Proof. (i) Here we apply Amann theory [56] to prove the local existence of $(u(x, t), v(x, t))$. In terms of $U = (u, v)^T$, the system (5) is written as

$$\begin{cases} \frac{\partial U}{\partial t} = \nabla \cdot (\mathcal{A}(U) \nabla U) + F(U), & x \in \Omega, t > 0, \\ \frac{\partial U}{\partial n} = (0, 0)^T, & x \in \partial\Omega, t > 0, \\ U(x, 0) = (u_0, v_0)^T, & x \in \Omega, \end{cases} \quad (12)$$

where

$$\mathcal{A}(U) = \begin{pmatrix} 1 & 0 \\ cv & d \end{pmatrix} \text{ and } F(U) = \begin{pmatrix} F_1(U) \\ F_2(U) \end{pmatrix}. \quad (13)$$

Since the matrix $\mathcal{A}(U)$ is positive definite, the system (5) is normally parabolic and the local existence of classical solutions follows from Theorem 7.3 in [56]. Thus, there exists a maximal existence time $T > 0$ such that the system (5) has a unique solution $(u(x, t), v(x, t)) \in C(\bar{\Omega} \times [0, T]) \cap C^{2,1}(\bar{\Omega} \times (0, T))$, with $u, v \geq 0$.

(ii) Let $K_1(t) = \int_{\Omega} u(x, t) dx$ and $K_2(t) = \int_{\Omega} v(x, t) dx$. Integrating the first equation and using no-flux boundary condition, we find

$$\frac{dK_1}{dt} = \int_{\Omega} F_1(u, v) dx \leq \int_{\Omega} (u - u^2) dx.$$

Using Hölder inequality, we find $\int_{\Omega} u^2 dx \geq \frac{1}{|\Omega|} \left(\int_{\Omega} u dx \right)^2$, which leads to

$$\frac{dK_1}{dt} \leq \left(K_1 - \frac{K_1^2}{|\Omega|} \right).$$

Therefore, $K_1(t) \leq \max \left\{ \|u_0\|_{L^1(\Omega)}, |\Omega| \right\} \equiv A$. We also have

$$\frac{d}{dt} (K_1 + eK_2) \leq \int_{\Omega} u dx - ef \int_{\Omega} v dx = -f(K_1 + eK_2) + (f+1)K_1.$$

Since $K_1 \leq A$, the above inequality leads to

$$K_2 \leq \frac{1}{e} (K_1 + eK_2) \leq \frac{1}{e} \left(\|u_0\|_{L^1(\Omega)} + e\|v_0\|_{L^1(\Omega)} + \frac{(f^2+1)}{f} A \right) \equiv B.$$

(iii) From (5), we have

$$\begin{cases} \frac{\partial u}{\partial t} = \nabla^2 u + F_1(u, v) \leq \nabla^2 u + u(1-u), & x \in \Omega, t > 0, \\ \frac{\partial u}{\partial n} = 0, & x \in \partial\Omega, t > 0, \\ u(x, 0) = u_0(x), & x \in \Omega. \end{cases}$$

Using the maximum principle for the parabolic equation [57], we have

$$0 \leq u(x, t) \leq \max \{ \|u_0\|_{L^\infty(\Omega)}, 1 \} \equiv C \text{ for all } x \in \Omega, t > 0.$$

Now, the second equation in (5) can be treated as a scalar linear equation in v . This implies $v(x, t) \geq 0$ for all $x \in \Omega, t > 0$. \square

Theorem 2. For any $(u_0, v_0) \in [W^{1,p}(\Omega)]^2$ with $u_0, v_0 \geq 0$ and $p > n$, the system (5) admits a unique global solution $(u(x, t), v(x, t)) \in [C(\bar{\Omega} \times [0, \infty)) \cap C^{2,1}(\bar{\Omega} \times (0, \infty))]^2 \equiv \mathcal{S}(\bar{\Omega})$ and the solution is uniformly bounded, i.e., there exists a constant $R(\|u_0\|_{L^\infty(\Omega)}, \|v_0\|_{L^\infty(\Omega)}) > 0$ such that

$$\|u(x, t)\|_{L^\infty(\Omega)} + \|v(x, t)\|_{L^\infty(\Omega)} \leq R(\|u_0\|_{L^\infty(\Omega)}, \|v_0\|_{L^\infty(\Omega)}) \text{ for all } t > 0.$$

Proof. We have already established $\|u(x, t)\|_{L^\infty(\Omega)} \leq C$ in Lemma 1(iii). However, we have obtained L_1 bound for $v(x, t)$ in Lemma 1(ii). To prove the theorem, we need to establish L_∞ bound for $v(x, t)$. The detailed steps are described below.

First, we establish the boundedness of $\|\nabla u\|_{L^\infty(\Omega)}$. Let $\{e^{t\nabla^2}\}_{t \geq 0}$ be the Neumann heat semigroup generated by $-\nabla^2$ and $\lambda_1 > 0$ be the first non-zero eigenvalue of $-\nabla^2$ in Ω . Then using the variation of constants formula for u , we get

$$u(x, t) = e^{t\nabla^2} u_0(x) + \int_0^t e^{(t-s)\nabla^2} F_1(u(x, s), v(x, s)) ds. \quad (14)$$

Using L^p - L^q estimates of Neumann heat semigroup (see Lemma 1.3 in [58]) and (14), we obtain

$$\begin{aligned} \|\nabla u(\cdot, t)\|_{L^\infty(\Omega)} &\leq \|\nabla e^{t\nabla^2} u_0\|_{L^\infty(\Omega)} + \int_0^t \|\nabla e^{(t-s)\nabla^2} F_1(u(\cdot, s), v(\cdot, s))\|_{L^\infty(\Omega)} ds \\ &\leq C_1 \left(1 + t^{-\frac{1}{2} - \frac{n}{2p}} \right) e^{-\lambda_1 t} \|u_0\|_{L^\infty(\Omega)} + \\ &\quad \int_0^t C_1 \left(1 + (t-s)^{-\frac{1}{2} - \frac{n}{2p}} \right) e^{-\lambda_1(t-s)} \|F_1(u(\cdot, s), v(\cdot, s))\|_{L^\infty(\Omega)} ds \\ &\leq C_2 \|u_0\|_{L^\infty(\Omega)} + C_3 \|F_1(u, v)\|_{L^\infty(\Omega)}, \end{aligned}$$

for some positive constant C_1, C_2 and C_3 . Since $\|F_1(u, v)\|_{L^\infty(\Omega)} \leq \frac{1}{4}$, we have $\|\nabla u\|_{L^\infty(\Omega)} \leq D(\|u_0\|_{L^\infty(\Omega)})$ for some positive constant $D(\|u_0\|_{L^\infty(\Omega)})$.

Next, we establish boundedness of $\|v\|_{L^q(\Omega)}$ where $q \geq 2$. Multiplying the second equation of (5) by v^{q-1} and integrating over Ω , we find

$$\int_{\Omega} v^{q-1} v_t dx - d \int_{\Omega} v^{q-1} \nabla^2 v dx = c \int_{\Omega} v^{q-1} \nabla \cdot (v \nabla u) dx + \int_{\Omega} v^{q-1} F_2(u, v) dx. \quad (15)$$

Using Gauss's divergence theorem and no-flux boundary conditions, we arrive at

$$\frac{1}{q} \frac{d}{dt} \int_{\Omega} v^q dx + d(q-1) \int_{\Omega} v^{q-2} |\nabla v|^2 dx = \int_{\Omega} v^{q-1} F_2(u, v) dx - c(q-1) \int_{\Omega} v^{q-1} \nabla v \cdot \nabla u dx.$$

Since

$$F_2(u, v) \leq \left(\frac{ea}{2\sqrt{b}} - f \right) v,$$

we finally find

$$\frac{1}{q} \frac{d}{dt} \int_{\Omega} v^q dx + d(q-1) \int_{\Omega} v^{q-2} |\nabla v|^2 dx \leq \left(\frac{ea}{2\sqrt{b}} - f \right) \int_{\Omega} v^q dx - c(q-1) \int_{\Omega} v^{q-1} \nabla v \cdot \nabla u dx. \quad (16)$$

Note that the inequality $\frac{|\vec{a}|^2}{2\varepsilon} + \frac{\varepsilon|\vec{b}|^2}{2} \geq \vec{a} \cdot \vec{b}$ holds for any $\varepsilon > 0$. Considering $\vec{a} = v^{\frac{q-2}{2}} \nabla v$, $\vec{b} = cv^{\frac{q}{2}} \nabla u$ and $\varepsilon = \frac{1}{d}$, we get

$$\frac{dv^{q-2} |\nabla v|^2}{2} + \frac{c^2 v^q |\nabla u|^2}{2d} \geq cv^{q-1} \nabla v \cdot \nabla u.$$

Using this inequality and the estimate $\|\nabla u\|_{L^\infty(\Omega)} \leq D(\|u_0\|_{L^\infty(\Omega)})$ (derived before) in (16), we get

$$\begin{aligned} \frac{1}{q} \frac{d}{dt} \int_{\Omega} v^q dx + f \int_{\Omega} v^q dx + \frac{d(q-1)}{2} \int_{\Omega} v^{q-2} |\nabla v|^2 dx &\leq \frac{ea}{2\sqrt{b}} \int_{\Omega} v^q dx + \frac{c^2(q-1)}{2d} \int_{\Omega} v^q |\nabla u|^2 dx \\ &\leq \left(\frac{ea}{2\sqrt{b}} + D^2 \right) \int_{\Omega} v^q dx \equiv K \int_{\Omega} v^q dx. \end{aligned} \quad (17)$$

For any $\varepsilon_1 > 0$, the inequality $\int_{\Omega} v^q dx \leq \varepsilon_1 \|\nabla v^{\frac{q}{2}}\|_2^2 + M$ holds for some $M > 0$ (see the Appendix

A). Using this in (17), we get

$$\frac{d}{dt} \int_{\Omega} v^q dx + fq \int_{\Omega} v^q dx + \frac{qd(q-1)}{2} \int_{\Omega} v^{q-2} |\nabla v|^2 dx \leq qK(\varepsilon_1 \|\nabla v^{\frac{q}{2}}\|_2^2 + M)$$

Using

$$\int_{\Omega} v^{q-2} |\nabla v|^2 dx = \frac{4}{q^2} \|\nabla v^{\frac{q}{2}}\|_2^2$$

in the above, we get

$$\frac{d}{dt} \int_{\Omega} v^q dx + fq \int_{\Omega} v^q dx \leq qK \left(\varepsilon_1 \|\nabla v^{\frac{q}{2}}\|_2^2 + M - \frac{2d(q-1)}{Kq^2} \|\nabla v^{\frac{q}{2}}\|_2^2 \right)$$

Setting $\varepsilon_1 = \frac{2d(q-1)}{Kq^2}$, we have

$$\frac{d}{dt} \int_{\Omega} v^q dx + fq \int_{\Omega} v^q dx \leq MqK,$$

which leads to

$$\|v\|_{L^q(\Omega)} \leq \left(\|v_0\|_{L^q(\Omega)}^q + \left(\frac{MK}{f} \right) \right)^{1/q} \equiv N.$$

Now using Sobolev embedding [59] and Moser–Alikakos iteration procedure [60], there exists a constant $P(\|u_0\|_{L^\infty(\Omega)}, \|v_0\|_{L^\infty(\Omega)}) > 0$ such that

$$\|v(\cdot, t)\|_{L^\infty(\Omega)} \leq P(\|u_0\|_{L^\infty(\Omega)}, \|v_0\|_{L^\infty(\Omega)}).$$

The proof is now complete. \square

3.2 Homogeneous steady-state analysis

Here, we discuss the stability of the homogeneous steady states. Note that a homogeneous steady-state $E(\tilde{u}, \tilde{v})$ of the system (12) corresponds to an equilibrium point (\tilde{u}, \tilde{v}) of the temporal system (6). Introducing $u(x, t) = \tilde{u} + \bar{u}(x, t)$ and $v(x, t) = \tilde{v} + \bar{v}(x, t)$, and linearizing about $E(\tilde{u}, \tilde{v})$, we find

$$\frac{\partial \bar{U}}{\partial t} = \mathcal{A}(E)\nabla^2 \bar{U} + J(E)\bar{U} \equiv \mathcal{L}(E)\bar{U},$$

where $\bar{U} \equiv (\bar{u}(x, t), \bar{v}(x, t)) \in [C(\bar{\Omega} \times [0, \infty)) \cap C^{2,1}(\bar{\Omega} \times (0, \infty))]^2$. Further, $J(E)$ and $\mathcal{A}(E)$ have been defined in (8) and (13) respectively.

Consider the eigenvalue problem

$$\begin{aligned} -\nabla^2 p &= kp \quad \text{in } \Omega, \\ \frac{\partial p}{\partial n} &= 0 \quad \text{on } \partial\Omega. \end{aligned} \tag{18}$$

For an eigenvalue k_i of the eigenvalue problem (18), let $E(k_i)$ be the corresponding eigenfunction space with $0 = k_0 < k_1 < \dots < k_i < \dots$. Further, assume that $\{\phi_{i,j} : j = 1, \dots, \dim(E(k_i))\}$ be an orthogonal basis set of $E(k_i)$ and $\mathcal{U}_{ij} = \{c\phi_{i,j} : c = (c_1, c_2)^T\}$. Let $\mathcal{U}_i = \bigoplus_{j=1}^{\dim(E(k_i))} \mathcal{U}_{ij}$ be the direct sum of \mathcal{U}_{ij} . It can be shown that

$$\mathcal{U} \equiv \left\{ (\phi, \psi)^T \in C^2(\bar{\Omega}) \times C^2(\bar{\Omega}) : \frac{\partial \phi}{\partial n} = \frac{\partial \psi}{\partial n} = 0 \text{ for } x \in \partial\Omega \right\} = \bigoplus_{i=1}^{\infty} \mathcal{U}_i, \tag{19}$$

and \mathcal{U}_i is invariant under the operator \mathcal{L} . Now, λ is an eigenvalue of \mathcal{L} if and only if λ is an eigenvalue of the matrix $\mathcal{L}_i = -k_i \mathcal{A}(E) + J(E)$ for some $i \geq 0$. The characteristic equation of \mathcal{L}_i is given by

$$\lambda^2 - T(k_i)\lambda + H(k_i) = 0, \tag{20}$$

where

$$\begin{aligned} T(k_i) &= a_{10} + b_{01} - (1+d)k_i, \\ H(k_i) &= dk_i^2 - \{a_{10}d + b_{01} - c\tilde{v}a_{01}\}k_i + (a_{10}b_{01} - a_{01}b_{10}). \end{aligned}$$

Now, from the principle of linearized stability of parabolic partial differential equation [61], the homogeneous steady state E is said to be locally asymptotically stable if $T(k_i) < 0$, and $H(k_i) > 0$ for all i .

Theorem 3. *The followings hold for the system (12):*

(a) *Trivial homogeneous steady-state $E_0(0,0)$ is always unstable.*

(b) *Axial homogeneous steady-state $E_1(1,0)$ is locally asymptotically stable if $f > f_{TC}$ and unstable if $f < f_{TC}$.*

(c) *Coexisting homogeneous steady state $E_1^*(u_1^*, v_1^*)$ is locally asymptotically stable if $a_{10} < \min \left\{ v_1^*, \frac{cv_1^*(u_1^* - 1) + v_1^*}{d} \right\} \equiv R_1$ and unstable if $a_{10} > v_1^*$.*

Proof. (a) For E_0 , we find $T(k_i) = 1 - f - (1 + d)k_i$ and $H(k_i) = dk_i^2 + (d + f)k_i - f$. Since $H(k_0) < 0$, E_0 is unstable.

(b) For E_1 , we have

$$T(k_i) = -1 + (f_{TC} - f) - (1 + d)k_i$$

and

$$H(k_i) = dk_i^2 + (d - (f_{TC} - f))k_i - (f_{TC} - f).$$

If $f > f_{TC}$, then $T(k_i) < 0$ and $H(k_i) > 0$ for all i . Thus, E_1 is locally asymptotically stable if $f > f_{TC}$. If $f < f_{TC}$, then $H(k_0) < 0$ and hence E_1 is unstable.

(c) If $a_{10} > -b_{01} = v_1^*$, then E_1^* is unstable since $T(k_0) > 0$. Now if $a_{10} < R_1$, then we find $a_{10} + b_{01} < 0$ and $a_{10}d + b_{01} - cv_1^*a_{01} < 0$. These conditions lead to

$$T(k_i) < 0 \text{ and } H(k_i) > 0 \text{ for all } i. \quad (21)$$

Hence, E_1^* is locally asymptotically stable if $a_{10} < R_1$. \square

Remark 1. Whenever homogeneous steady state E_2^* exists, it is unstable since $H(k_0) < 0$. In case of E_3^* (when it exists), it is locally asymptotically stable if $T(k_i) < 0$ and $H(k_i) > 0$ for all i . It is unstable if either of these conditions does not hold for some i .

3.3 Turing instability

In the case of Turing instability, the coexisting equilibrium point is asymptotically stable for the temporal system (6). But the corresponding homogeneous steady state of the spatio-temporal model (5) becomes unstable under spatial perturbation. Thus, $T(k_i) < 0$ and $H(k_i) > 0$ for $i = 0$, but at least one of these conditions is violated for some $i \geq 1$. Note that $T(k_i) < T(k_0)$ for all $i \geq 1$. Hence, for Turing instability, there exists some k_i ($i \geq 1$) for which $H(k_i) < 0$. The eigenvalues k_i are discrete for a bounded Ω . To find the Turing bifurcation threshold, we consider an unbounded domain for which a continuous spectrum of eigenvalues is obtained. Hence, the Turing instability condition becomes $H(k) < 0$ for some $k \neq 0$. Here, we consider the homogeneous steady state corresponding to the coexisting equilibrium point $E_1^*(u_1^*, v_1^*)$.

The minimum value of $H(k)$ is

$$H_{min} = \frac{-a_{10}^2 d^2 + ((2a_{10}cv_1^* - 4b_{10})a_{01} + 2a_{10}b_{01})d - (a_{01}cv_1^* - b_{01})^2}{4d},$$

which occurs at wavenumber

$$k_{min} = \frac{a_{10}d + b_{01} - a_{01}cv_1^*}{2d}.$$

Now, at the threshold of the Turing bifurcation, we have $H_{min} = 0$ at critical wavenumber $k_T = k_{min}$, and the corresponding critical Turing value c_T of c is determined as follows

$$c_T = \frac{a_{10}d + b_{01} - 2\sqrt{d \det(J)}}{a_{01}v_1^*}. \quad (22)$$

The system becomes Turing unstable for $c > c_T$. We plot the Turing surface boundary in the f - d - c space for parameter values $a = 7$, $b = 5.65$, and $e = 0.95$ (see Fig. 7). The Turing instability sets in above the Turing boundary surface. In front of the Hopf surface, we have an additional Hopf instability. These two instabilities, divide the f - c - d space into four regions: (i) a stable region below the Turing boundary surface and behind the Hopf plane, (ii) a Turing region above the Turing boundary surface and behind the Hopf plane, (iii) a Hopf region below the Turing boundary surface and in front of the Hopf plane, and (iv) a Turing-Hopf region above the Turing boundary surface and in front of the Hopf plane. We will discuss the spatio-temporal dynamics in these regions in the section 5.

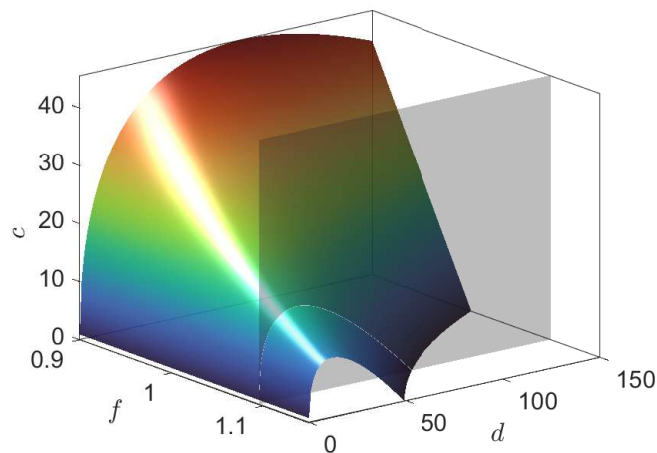


Figure 7: Turing boundary surface (coloured surface) and Hopf plane (grey vertical plane) in the f - d - c space. Note that the system (5) exhibits Turing instability above the coloured surface and Hopf instability in front of the grey plane. The values of the other parameters are $a = 7$, $b = 5.65$, and $e = 0.95$.

4 Weakly nonlinear analysis

Here, we perform weakly nonlinear analysis using the method of multiple scales near the Turing bifurcation threshold ($c = c_T$). We derive the amplitude equations for the Turing solutions, which also shows the existence of non-homogeneous stationary solutions near the Turing thresholds. For simplicity, we consider one-dimensional spatial domain as $\Omega = [0, L] \in \mathbb{R}$. First, we employ a Taylor series expansion up to the third order to expand the system (5) around $E_*^1(u_*^1, v_*^1)$

$$\frac{\partial \mathbf{W}}{\partial t} = \mathcal{L}^c \mathbf{W} + \mathcal{N} + \frac{1}{2} \mathcal{B}(\mathbf{W}, \mathbf{W}) + \frac{1}{6} \mathcal{T}(\mathbf{W}, \mathbf{W}, \mathbf{W}) \equiv \mathcal{Z}(\mathbf{W}), \quad (23)$$

where

$$\mathbf{W} = \begin{pmatrix} u - u_*^1 \\ v - v_*^1 \end{pmatrix}, \quad \mathcal{L}^c = \begin{pmatrix} a_{10} + \partial_{xx} & a_{01} \\ b_{10} + cv_1^* \partial_{xx} & b_{01} + d \partial_{xx} \end{pmatrix}, \quad \text{and} \quad \mathcal{N} = \begin{pmatrix} 0 \\ c(v \nabla^2 u + \nabla u \cdot \nabla v) \end{pmatrix}$$

denote the perturbation vector, linear operator, and nonlinear prey-taxis term, respectively. Further, the bi-linear operator \mathcal{B} and tri-linear operator \mathcal{T} are defined as

$$\mathcal{B}(\mathbf{P}_1, \mathbf{P}_2) = \begin{pmatrix} \sum_{i,j \in \{1,2\}} \frac{\partial^2 F_1}{\partial y_i \partial y_j} \Big|_{(u_*^1, v_*^1)} P_1^{(i)} P_2^{(j)} \\ \sum_{i,j \in \{1,2\}} \frac{\partial^2 F_2}{\partial y_i \partial y_j} \Big|_{(u_*^1, v_*^1)} P_1^{(i)} P_2^{(j)} \end{pmatrix},$$

$$\mathcal{T}(\mathbf{P}_1, \mathbf{P}_2, \mathbf{P}_3) = \begin{pmatrix} \sum_{i,j,k \in \{1,2\}} \frac{\partial^2 F_1}{\partial y_i \partial y_j \partial y_k} \Big|_{(u_*^1, v_*^1)} P_1^{(i)} P_2^{(j)} P_3^{(k)} \\ \sum_{i,j,k \in \{1,2\}} \frac{\partial^2 F_2}{\partial y_i \partial y_j \partial y_k} \Big|_{(u_*^1, v_*^1)} P_1^{(i)} P_2^{(j)} P_3^{(k)} \end{pmatrix},$$

where $\mathbf{P}_m = \begin{pmatrix} P_m^{(1)} \\ P_m^{(2)} \end{pmatrix}$, for $m = 1, 2, 3$; $y_1 = u$ and $y_2 = v$.

We introduce slow time scale $\tau = \varepsilon^2 t$, where ε measures the distance between prey-taxis parameter c and the critical Turing threshold c_T as $c = c_T + \varepsilon^2 c_2$. We also expand the solution of the system (23) in terms of ε as

$$\mathbf{W} = \varepsilon \mathbf{W}_1 + \varepsilon^2 \mathbf{W}_2 + \varepsilon^3 \mathbf{W}_3 + O(\varepsilon^4).$$

Accordingly, the operator \mathcal{L}^c , \mathcal{B} and \mathcal{T} in (23) can be expressed as

$$\mathcal{L}^c = \mathcal{L}^{c_T} + \varepsilon^2 c_2 v_*^1 \begin{pmatrix} 0 & 0 \\ 1 & 0 \end{pmatrix} \nabla^2 + O(\varepsilon^4),$$

$$\mathcal{B}(\mathbf{W}, \mathbf{W}) = \varepsilon^2 \mathcal{B}(\mathbf{W}_1, \mathbf{W}_1) + 2\varepsilon^3 \mathcal{B}(\mathbf{W}_1, \mathbf{W}_2) + O(\varepsilon^4),$$

$$\mathcal{T}(\mathbf{W}, \mathbf{W}, \mathbf{W}) = \varepsilon^3 \mathcal{T}(\mathbf{W}_1, \mathbf{W}_1, \mathbf{W}_1) + O(\varepsilon^4).$$

Substituting all the above expansions into (23), we obtain a series of equations in \mathbf{W}_i ($i = 1, 2, \dots$) by collecting the terms at each order in ε . Each of these equations is subjected to the Neumann boundary condition.

At $O(\varepsilon)$, we have $\mathcal{L}^{c_T} \mathbf{W}_1 = 0$, whose solution is

$$\mathbf{W}_1 = A(\tau) \Phi \cos(k_T x) \quad \text{with } \Phi \in \text{Ker}(J(E_1^*) - k_T^2 D^{c_T}).$$

Here, $A(\tau)$ is the amplitude of the growing pattern, unknown at the moment. We normalize Φ vector as

$$\Phi = \begin{pmatrix} 1 \\ \phi \end{pmatrix} \quad \text{with } \phi = \frac{k_T^2 - a_{10}}{a_{01}}.$$

At $O(\varepsilon^2)$, we obtain

$$\mathcal{L}^{c_T} \mathbf{W}_2 = (\mathbf{h}_{20} + \mathbf{h}_{22} \cos(2k_T x)) A^2 \equiv \mathbf{H}, \quad (24)$$

where $\mathbf{h}_{20} = -\frac{1}{4} \mathcal{B}(\Phi, \Phi)$, $\mathbf{h}_{22} = -\frac{1}{4} \mathcal{B}(\Phi, \Phi) + c_T k_T^2 \begin{pmatrix} 0 \\ \phi \end{pmatrix}$. Using Fredholm alternative theorem,

the system (24) has a solution when $\langle \mathbf{H}, \Psi \rangle \equiv \int_0^L \mathbf{H} \Psi \, dx = 0$, where $\Psi = \begin{pmatrix} \psi \\ 1 \end{pmatrix} \cos(k_T x) \in$

$\text{Ker}(\mathcal{L}^{c_T})^\dagger$ with $\psi = \frac{dk_T^2 - b_{01}}{a_{01}}$. Note that A^\dagger denotes the adjoint of the operator A . Note that here the Fredholm alternative theorem automatically holds. The solution of (24) is given by

$$\mathbf{W}_2 = (\mathbf{k}_{20} + \mathbf{k}_{22} \cos(2k_T x))A^2,$$

where $J(E_1^*)\mathbf{k}_{20} = \mathbf{h}_{20}$ and $(J(E_1^*) - 4k_T^2 D^{c_T})\mathbf{k}_{22} = \mathbf{h}_{22}$.

At $O(\varepsilon^3)$, we find

$$\mathcal{L}^{c_T} \mathbf{W}_3 = \left(\frac{dA}{d\tau} \Phi + \mathbf{g}_{11} A + \mathbf{g}_{31} A^3 \right) \cos(k_T x) + \mathbf{g}_{33} \cos(3k_T x) A^3 \equiv \mathbf{G}, \quad (25)$$

where

$$\mathbf{g}_{11} = c_2 k_T^2 v_1^* \begin{pmatrix} 0 \\ 1 \end{pmatrix}, \quad \mathbf{g}_{31} = -\mathcal{B}(\Phi, \mathbf{k}_{20}) - \frac{1}{2} \mathcal{B}(\Phi, \mathbf{k}_{22}) - \frac{1}{8} \mathcal{J}(\Phi, \Phi, \Phi) + c_T k_T^2 \begin{pmatrix} 0 \\ k_{20}^{(1)} \phi + k_{22}^{(1)} - \frac{1}{2} k_{22}^{(2)} \end{pmatrix},$$

$$\text{and } \mathbf{g}_{33} = -\frac{1}{2} \mathcal{B}(\Phi, \mathbf{k}_{22}) - \frac{1}{24} \mathcal{J}(\Phi, \Phi, \Phi) + c_T k_T^2 \begin{pmatrix} 0 \\ 3k_{22}^{(1)} \phi + \frac{3}{2} k_{22}^{(2)} \end{pmatrix}.$$

Using Fredholm alternative theorem in equation (25), we obtain $\langle \mathbf{G}, \Psi \rangle = 0$, which leads to the cubic Stuart-Landau equation

$$\frac{dA}{d\tau} = \sigma A - l A^3, \quad (26)$$

where

$$\sigma = -\frac{\langle \mathbf{g}_{11}, \Psi \rangle}{\langle \Phi, \Psi \rangle} \quad \text{and} \quad l = \frac{\langle \mathbf{g}_{31}, \Psi \rangle}{\langle \Phi, \Psi \rangle}.$$

Here, σ is always positive and (26) is similar to normal form of pitchfork bifurcation.

Supercritical case

If $l > 0$, then the system (26) has two stable fixed points $A_* = \pm \sqrt{\frac{\sigma}{l}}$ and an unstable fixed point $A_* = 0$. These stable fixed points represent the Turing pattern with wavenumber k_T for $c > c_T$ and all non-zero solutions approach them after a long time, i.e.,

$$\lim_{t \rightarrow \infty} A(t) \equiv A_\infty = \pm \sqrt{\frac{\sigma}{l}}.$$

Therefore, the final solution of (23) is $\mathbf{U}_\infty(x) = \sqrt{c - c_T} A_\infty \Phi \cos(k_T x) + O(\varepsilon^2)$ for $c > c_T$.

Subcritical case

For $l < 0$, the system (26) does not admit any nontrivial equilibrium solution. Here, we need to include higher order terms in the expansion. Thus, we employ a Taylor series expansion up to the fifth order to expand the system (5) around $E_*^1(u_*^1, v_*^1)$

$$\frac{\partial \mathbf{W}}{\partial t} = \mathcal{Z}(\mathbf{W}) + \frac{1}{24} \mathcal{Q}(\mathbf{W}, \mathbf{W}, \mathbf{W}, \mathbf{W}) + \frac{1}{60} \mathcal{P}(\mathbf{W}, \mathbf{W}, \mathbf{W}, \mathbf{W}, \mathbf{W}), \quad (27)$$

where \mathcal{Q} and \mathcal{P} are the quad-linear operator and penta-linear operator defined similar to \mathcal{B} and \mathcal{J} . We also modify the multiple time scales $t = t(\tau, \tau_1)$, where $\tau = \varepsilon^2 t$ and $\tau_1 = \varepsilon^4 t$; c and \mathbf{W} up to the fifth order of ε as

$$c = c_T + \varepsilon^2 c_2 + \varepsilon^4 c_4 + O(\varepsilon^6),$$

$$\mathbf{W} = \varepsilon \mathbf{W}_1 + \varepsilon^2 \mathbf{W}_2 + \varepsilon^3 \mathbf{W}_3 + \varepsilon^4 \mathbf{W}_4 + \varepsilon^5 \mathbf{W}_5 + O(\varepsilon^6).$$

The right hand side of (25) using (26) becomes

$$G = (\mathbf{G}_{11}A + \mathbf{G}_{13}A^3) \cos(k_T x) + \mathbf{G}_{33} \cos(3k_T x)A^3,$$

where $\mathbf{G}_{11} = \mathbf{g}_{11} + \sigma A \Phi$, $\mathbf{G}_{13} = \mathbf{g}_{13} - lA^3 \Phi$, and $\mathbf{G}_{33} = \mathbf{g}_{33}$. Note that the amplitude now becomes $A = A(\tau, \tau_1)$. The solution of (25) is given by

$$\mathbf{W}_3 = (\mathbf{C}_{11} + \mathbf{C}_{13}A^2)A \cos(k_T x) + \mathbf{C}_{33} \cos(3k_T x)A^3,$$

where $(J(E_1^*) - k_T^2 D^{cT}) \mathbf{C}_{11} = \mathbf{G}_{11}$, $(J(E_1^*) - k_T^2 D^{cT}) \mathbf{C}_{13} = \mathbf{G}_{13}$, and $(J(E_1^*) - 9k_T^2 D^{cT}) \mathbf{C}_{33} = \mathbf{G}_{33}$.

At $O(\varepsilon^4)$, we obtain

$$\mathcal{L}^{cT} \mathbf{W}_4 = \mathbf{H}_{20}A^2 + \mathbf{H}_{22}A^2 \cos(2k_T x) + \mathbf{H}_{40}A^4 + \mathbf{H}_{42}A^4 \cos(2k_T x)A^2 + \mathbf{H}_{44}A^4 \cos(4k_T x) \equiv \mathbf{H}, \quad (28)$$

Again the Fredholm alternative condition automatically holds due to the choice of our perturbation. Further solving (28), we find

$$\mathbf{W}_4 = \mathbf{D}_{20}A^2 + \mathbf{D}_{22}A^2 \cos(2k_T x) + \mathbf{D}_{40}A^4 + \mathbf{D}_{42}A^4 \cos(2k_T x)A^2 + \mathbf{D}_{44}A^4 \cos(4k_T x),$$

where $J(E_1^*)\mathbf{D}_{20} = \mathbf{H}_{20}$, $(J(E_1^*) - 4k_T^2 D^{cT})\mathbf{D}_{22} = \mathbf{H}_{22}$, $J(E_1^*)\mathbf{D}_{40} = \mathbf{H}_{40}$, $(J(E_1^*) - 4k_T^2 D^{cT})\mathbf{D}_{42} = \mathbf{H}_{42}$, and $(J(E_1^*) - 16k_T^2 D^{cT})\mathbf{D}_{44} = \mathbf{H}_{44}$.

Finally, at $O(\varepsilon^5)$, we obtain

$$\mathcal{L}^{cT} \mathbf{W}_5 = \frac{\partial A}{\partial \tau_1} \Phi + \mathbf{I}_{11}A \cos(k_T x) + \mathbf{I}_{31}A^3 \cos(k_T x) + \mathbf{I}_{51}A^5 \cos(k_T x) + \mathbf{I}^* \equiv \mathbf{I}, \quad (29)$$

where \mathbf{I}^* contains the orthogonal terms of \mathbf{W}_1 in \mathbf{I} . Further, \mathbf{H}_{ij} and \mathbf{I}_{ij} are explicitly computed in terms of the system parameters. As these expressions are quite involved, we omit them for the sake of brevity.

Using the Fredholm solvability condition once more in (29), we arrive at a quintic Stuart-Landau equation

$$\frac{\partial A}{\partial \tau_1} = \sigma' A - l' A^3 + \rho' A^5, \quad (30)$$

where

$$\sigma' = -\frac{\langle \mathbf{I}_{11}, \bar{\Phi} \rangle}{\langle \Phi, \bar{\Phi} \rangle}, \quad l' = \frac{\langle \mathbf{I}_{31}, \bar{\Phi} \rangle}{\langle \Phi, \bar{\Phi} \rangle} \quad \text{and} \quad \rho' = -\frac{\langle \mathbf{I}_{51}, \bar{\Phi} \rangle}{\langle \Phi, \bar{\Phi} \rangle}.$$

Adding (26) and (30), we finally obtain

$$\frac{dA}{dt} = \varepsilon^2 (\hat{\sigma} A - \hat{l} A^3 + \hat{\rho} A^5), \quad (31)$$

where $\hat{\sigma} = \sigma + \varepsilon^2 \sigma'$, $\hat{l} = l + \varepsilon^2 l'$ and $\hat{\rho} = \varepsilon^2 \rho'$. If $\hat{\sigma} > 0$, $\hat{l} < 0$ and $\hat{\rho} < 0$, then equation (31) admits two stable equilibria $\pm \sqrt{\frac{\hat{\sigma} - \sqrt{\hat{\sigma}^2 - 4\hat{\rho}\hat{l}}}{2\hat{\rho}}}$. Thus, we obtain the amplitude of the stationary pattern solution for $c > c_T$.

5 Numerical results

Here, we first validate the results of weakly nonlinear analysis (WNA) and then discuss the effects of prey-taxis parameter c on the Turing solutions. Next we investigate spatio-temporal transient dynamics and non-homogeneous oscillatory solution in the Hopf region.

5.1 Validation of WNA results

We take the parameter values $a = 7$, $b = 5.65$, $e = 0.95$, $f = 0.98$, and $d = 80$. For this parameter set, the coexisting homogeneous steady state $E_1^*(0.210978, 0.141065)$ is asymptotically stable under homogeneous perturbation. The corresponding Turing threshold is $c_T = 26.889081$ with critical wave number $k_T = 0.283128$. Using WNA, we find the cubic Stuart-Landau equation

$$\frac{dA}{d\tau} = 0.054965A + 2.925863A^3, \quad (32)$$

which shows the subcritical nature of the bifurcation. Extending WNA up to the fifth order, we obtain quintic Stuart-Landau equation

$$\frac{\partial A}{\partial \tau_1} = -0.000463A + 6.926411A^3 - 43.690556A^5. \quad (33)$$

Using (32) and (33), we obtain the amplitude equation

$$\frac{dA}{dt} = \varepsilon^2(\hat{\sigma}A - \hat{l}A^3 + \hat{\rho}A^5), \quad (34)$$

where $\hat{\sigma} = 0.054965 - 0.000463\varepsilon^2$, $\hat{l} = -(2.925863 + 6.926411\varepsilon^2)$, and $\hat{\rho} = -43.690556\varepsilon^2$. The equilibrium amplitude A_∞ of the Turing pattern solution at $c = c_T(1 + \varepsilon^2)$ satisfies $\hat{\sigma} - \hat{l}A^2 + \hat{\rho}A^4 = 0$, and the stationary solution of u up to third order is

$$u_\infty(x) = u_1^* + \varepsilon A_\infty \cos(k_T x) + \varepsilon^2 A_\infty^2 (1.8 + 1.811195 \cos(k_T x)) + \varepsilon^3 A_\infty ((1 + A_\infty^2) \cos(k_T x) + 1.969026 \cos(3k_T x)). \quad (35)$$

We have plotted $u_\infty(0)$ against the prey-taxis parameter c in Fig. 8. For $c > c_T$, the system (5) has two stable branches of pattern solution and the unstable homogeneous stationary solution (HSS). We plot both the stable branches for $c = 27$ and compared them with the numerical solutions in Fig. 9. The amplitudes of both solutions are in good agreement. For $21.1348 < c < c_T$, we

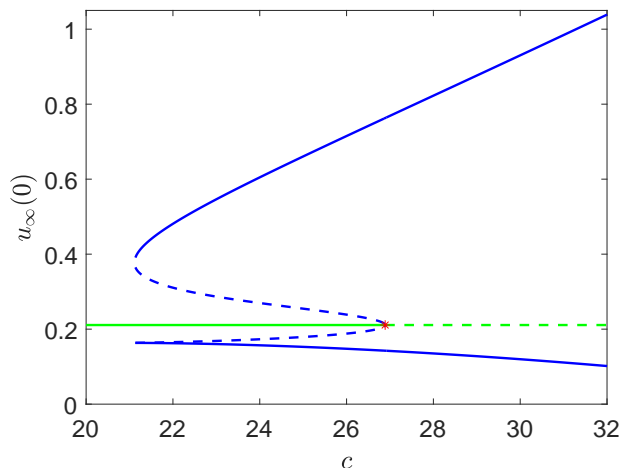


Figure 8: Plot of the solution up to third order from the weakly nonlinear analysis. Here green and blue color curves denote homogeneous stationary solution and pattern solution, respectively. The solid and dashed curves respectively correspond to the stable and unstable branches. Other parameter values are $a = 7$, $b = 5.65$, $f = 0.98$, $e = 0.95$, $d = 80$ and $k_T = 0.283128$.

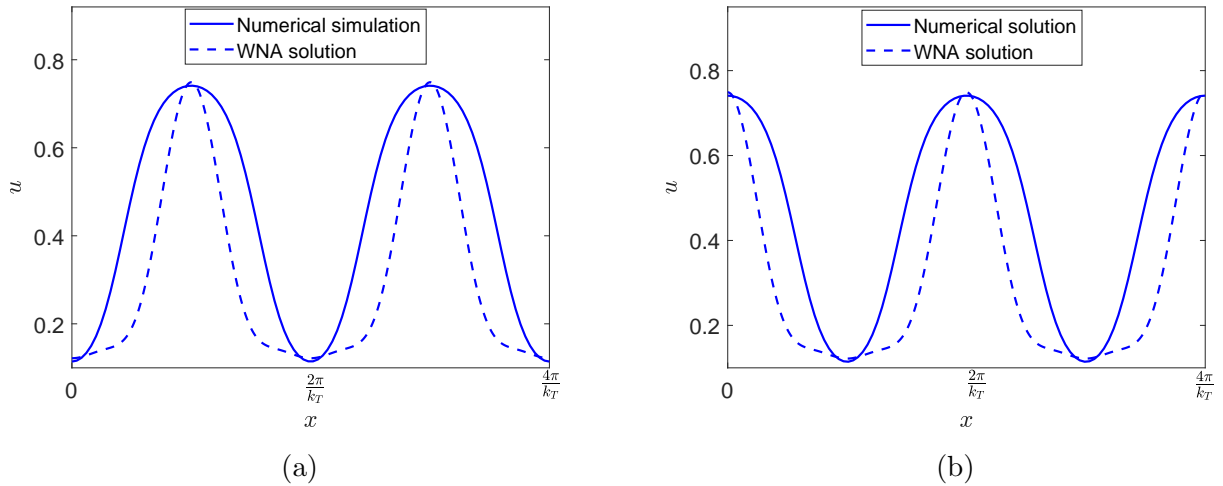


Figure 9: Comparison of solution up to third order from weakly nonlinear analysis and numerical solution: (a) lower branch, (b) upper branch. The values of other parameters are $a = 7$, $b = 5.65$, $f = 0.98$, $e = 0.95$, $d = 80$, $c = 27$ and $k_T = 0.283128$.

have two unstable branches of pattern solution, two stable branches of pattern solution and the stable HSS. When $21.1348 < c < c_T$, numerical computation under random perturbation about the homogeneous steady state leads to the HSS, but a backward continuation of pattern solution from $c > c_T$ leads to the stable pattern solution. Thus, the system (5) shows hysteresis cycle [12, 62] in this parameter range.

5.2 Effect of prey-taxis c on Turing solution

In subsection 3.3, we have observed the appearance of the Turing pattern when the prey-taxis coefficient c crosses a threshold c_T . If we consider the parameter values $a = 7$, $b = 5.65$, $f = 0.95$, $e = 0.95$ and $d = 100$, then the corresponding Turing threshold is $c_T = 31.4793$. We simulate the spatio-temporal model with a small amplitude spatial perturbation around the coexisting homogeneous steady state $E_1^* = (0.2016, 0.1402)$. The system shows a stable homogeneous steady state for $c < c_T$ and a non-homogeneous Turing solution for $c > c_T$. We plot the stationary Turing solutions of u and v for $c = 35$ and $c = 50$ in Fig. 10. Since the predator population avoid high prey density areas, the peak of the prey population corresponds to the trough of the predator population. As the value of c increases from $c = 35$ to $c = 50$, the peak prey density also increases due to the group defense of the prey population. Consequently, the trough of the predator population decreases further (see Fig. 10).

Another important findings is the effects of the prey-taxis c on the spatial averages of the populations. The spatial average of the prey population jumps from 0.2016 for $c < c_T$ to 0.4516 for $c = 35$. Thus, the spatial average of the prey population becomes more than doubled due to Turing bifurcation. On the other hand, the predator population changes from 0.1402 for $c < c_T$ to 0.1582 for $c = 35$, a modest increase compared to prey population. Interestingly, the spatial average of the prey increases and that of predator decreases as c is increased from $c = 35$ to $c = 50$. Thus, an increase prey-taxis is beneficial to the prey species compared to the predator species.

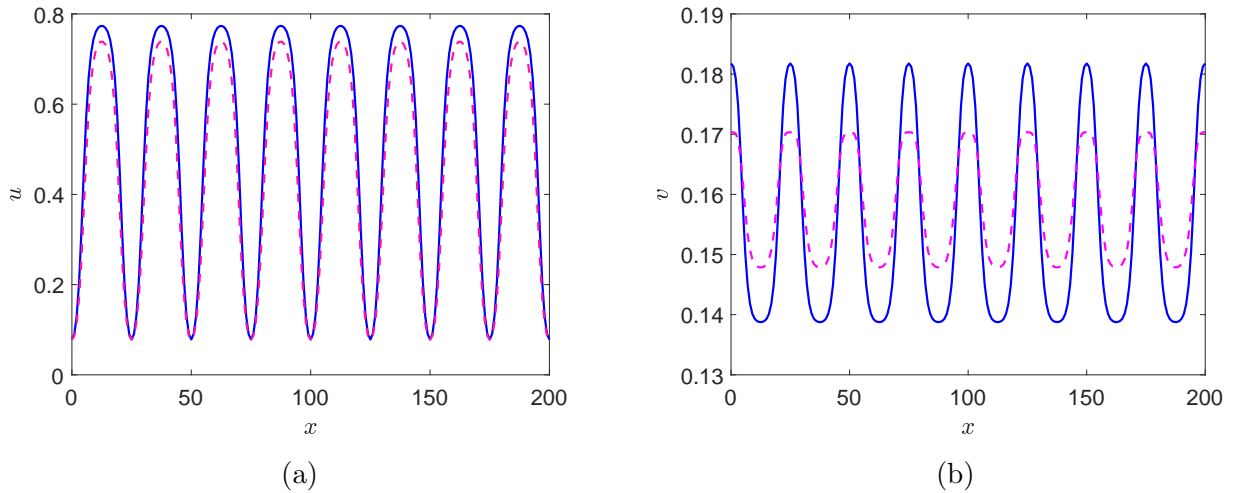


Figure 10: Effect of prey-taxis c on stationary Turing solutions: (a) prey solutions, (b) predator solutions. Here magenta dashed and blue solid curves denote the corresponding stationary Turing solutions for $c = 35$ and $c = 50$, respectively. The values of other parameters are $a = 7$, $b = 5.65$, $f = 0.95$, $e = 0.95$, and $d = 100$.

5.3 Spatio-temporal transient dynamics

Here, we discuss taxis induced transient solutions for the system (5). We choose the parameter values $a = 7$, $b = 5.65$, $f = 1.07$, $e = 0.95$, and $d = 80$. For this parameter set, we calculate $c_T = 5.552$ using (22). Note that the corresponding temporal system has bistability between coexisting equilibrium point E_1^* and axial equilibrium point E_1 . For $c = 5$, the system (5) is neither Turing unstable nor Hopf unstable. Hence, the system reaches the homogeneous steady-state solution E_1^* after the initial transients for $c = 5$ when simulated with random perturbation around E_1^* . However, for $c > c_T$, we observe Turing instability. Usually, the system settles down to a stationary non-homogeneous state in Turing unstable domain. However, for $c = 6 > c_T$, we find that the system ultimately settles down to homogeneous steady predator-free state E_1 (see Fig. 11). The system initially evolves towards the Turing solution and the intermediate Turing solution satisfies the corresponding dispersion relation $H(k^2) < 0$ for this parameter value. Though the Turing solution persists for considerable amount of time, but it ultimately becomes unstable leading to the homogeneous steady predator-free state. Interestingly, for lower values of c with $c < c_T$, coexistence occurs, whereas higher value of c with $c > c_T$ leads to the extinction of the predator species [see Fig. 11(c)]. Thus, the extinction described is induced by the prey-taxis.

Next, we examine the effects of the diffusion and taxis on the long transient and hysteresis states observed in the temporal model (see Fig. 5). We consider the same parameter values as in Fig. 5(a) together with the diffusion parameter $d = 80$, taxis parameter $c = 40$, and a domain of length $L = 200$. The initial condition is chosen as

$$u(x, 0) = \begin{cases} 1.4 + 0.01\xi(x), & \text{for } |x - 100| < 50, \\ 1.4, & \text{otherwise,} \end{cases}, \quad v(x, 0) = \begin{cases} 0.05 + 0.01\xi(x), & \text{for } |x - 100| < 50, \\ 0.05, & \text{otherwise.} \end{cases}$$

Here, $\xi(x)$ is the Gaussian noise function. We choose this specific initial condition in order to compare our solution with the temporal solution. The corresponding spatio-temporal dynamics is shown in Fig. 12. We plot the spatial average $\langle u \rangle$ of the prey population for the system (5) against time in Fig. 12(b). We have also shown their corresponding variation u of the temporal model (6). It shows that the transient time for both systems is almost the same, although their

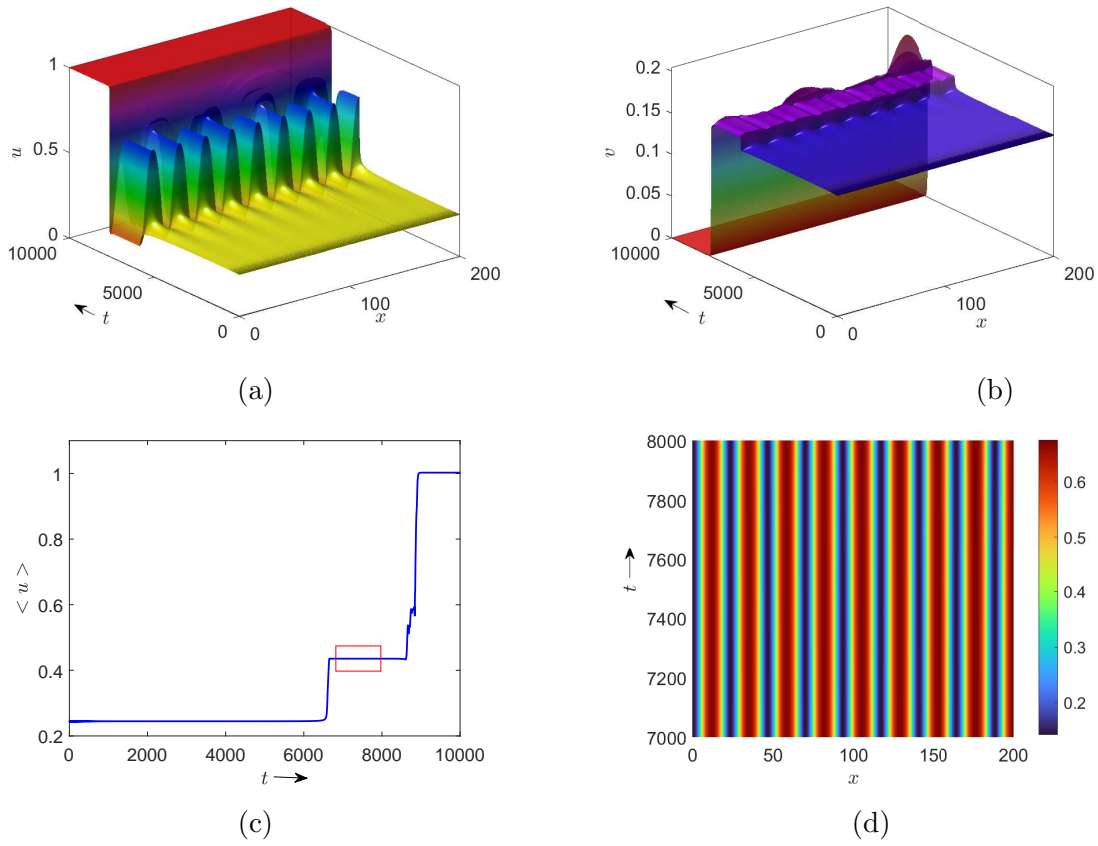


Figure 11: Transient dynamics leading to homogeneous steady predator-free state for $c = 6$: (a) space-time plot of the prey species, (b) space-time plot of the predator species, (c) spatial average of prey species against time, (d) persistence of Turing solution during intermediate stage. Other parameter values are $a = 7$, $b = 5.65$, $e = 0.95$, $f = 1.07$, and $d = 80$.

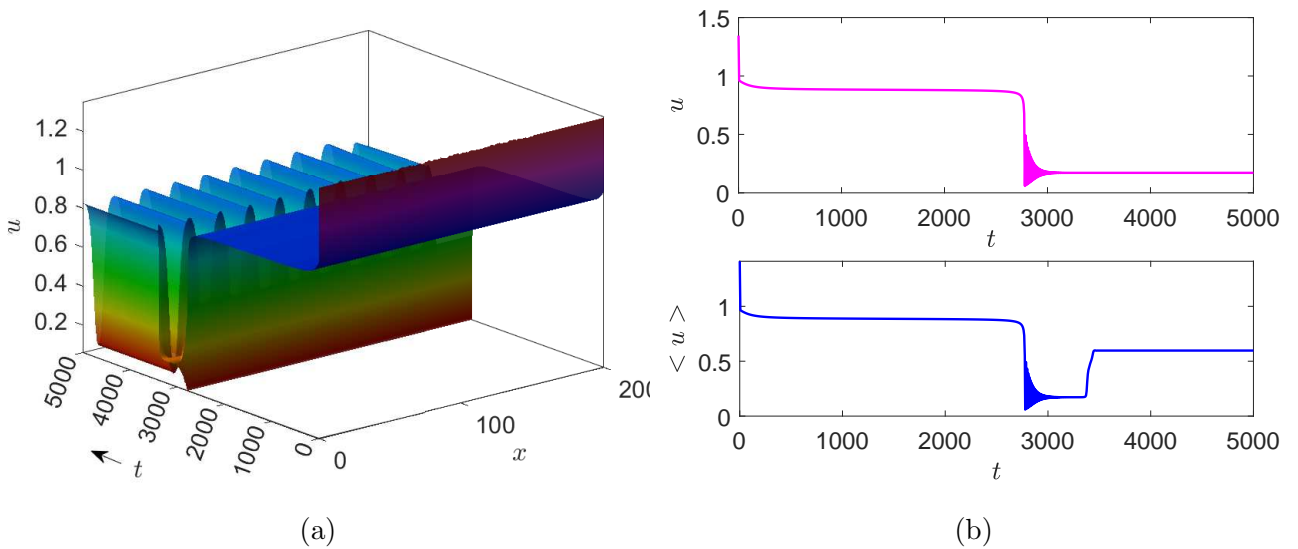


Figure 12: Effects of the diffusion and taxis on the long transient dynamics of the temporal model: (a) space-time plot of the prey species u , (b) variation of the temporal solution u of (6) and the spatial average of the spatio-temporal model (5) against time. The values of other parameters are $a = 7$, $b = 7$, $e = 0.95$, $f = 0.8013$, $d = 80$, and $c = 40$.

final destination is different. In contrast to the temporal system, the space-time solution evolves to a Turing pattern due to Turing instability.

Finally, we discuss the effects of the diffusion and taxis on the long oscillatory transient dynamics observed in the temporal model [see Fig. 6(b)]. For this purpose, we consider the initial condition similar to that mentioned above together with $d = 80$ and $c = 40$. However, the long oscillatory transient dynamics does not appear for the spatio-temporal solution. Figure 13 shows that the predator becomes extinct in a short time and the solution approaches homogeneous steady predator-free state E_1 .

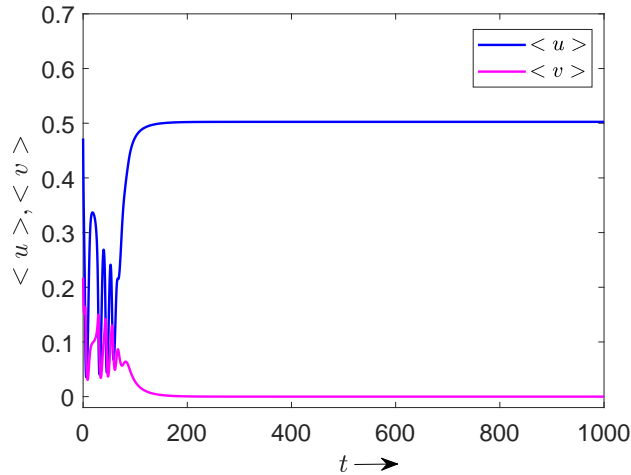


Figure 13: Variation of the spatial averages of the prey and predator populations against time. The values of other parameters are $a = 7$, $b = 7$, $e = 0.95$, $f = 0.867682$, $d = 80$, and $c = 40$.

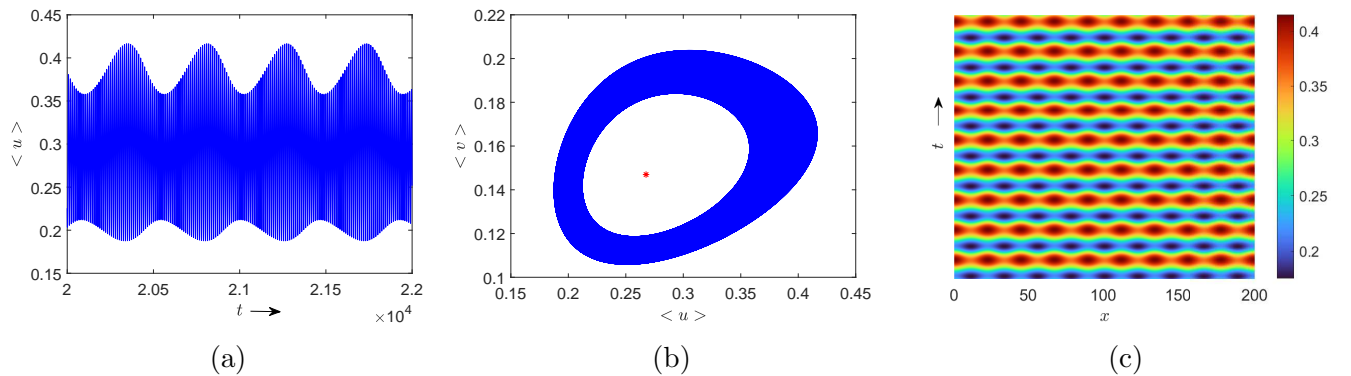


Figure 14: Time oscillatory and spatially non-homogeneous solution: (a) variation of spatial average $\langle u \rangle$ against time, (b) phase portrait of spatial averages $\langle u \rangle$ and $\langle v \rangle$, (c) contour plot of space-time solution u after the initial transient. The values of other parameters are $a = 7$, $b = 5.65$, $e = 0.95$, $f = 1.12$, $d = 40$, and $c = 5$.

5.4 Oscillatory solution

Apart from the homogeneous and non-homogeneous steady-state solutions, the spatio-temporal system (5) also exhibits oscillatory solutions in the Hopf region. The parameter values $a = 7$, $b = 5.65$, $e = 0.95$, $f = 1.12$, $d = 40$, and $c = 5$ lie in the Hopf region. Note that the temporal system (6) exhibits bistability between the periodic solution around E_1^* and the axial equilibrium E_1 with

the associated temporal parameters from this set. The corresponding spatio-temporal system (23) shows an oscillatory in time and non-homogeneous in space solution shown in Fig. 14. The phase portrait of spatial averages $\langle u \rangle$ and $\langle v \rangle$ [see Fig. 14(b)] confirms the quasi-periodic nature of the solution. The parameter set moves into the Turing-Hopf region with an increase in c , and the predator species becomes extinct leading to the homogeneous steady predator-free state. This final state corresponds to the axial equilibrium of the bistable states and it is similar to the taxis-induced extinction discussed earlier. The parameter set moves well inside the Hopf region with a decrease in c . The system now exhibits a homogeneous oscillatory solution corresponding to the stable periodic solution around E_1^* .

6 Conclusion

The primary goal of our work is to investigate the effects of group defense among prey species on the spatio-temporal distribution of both the prey and predator populations modelled by a Bazykin-type prey-predator model. The group defense of the prey species is incorporated using a non-monotonic functional response in the temporal model. Due to group defense, the predator species avoid areas with high prey density. We also include repellent prey-taxis to take into account this response of the predator species. The temporal model (6) exhibits a range of complex dynamics, including bistability, tristability, global bifurcations, and long transient dynamics. The corresponding spatio-temporal system (5) possesses global bounded solutions. Existence of non-homogeneous stationary solution above the Turing threshold c_T has been established using WNA. Further, exhaustive numerical simulations have been performed to validate the results of WNA and to investigate long transient dynamics present in the spatio-temporal systems.

We have used bifurcation analysis on the temporal system (6) to identify various local and global bifurcations by considering b and f as bifurcation parameters. Note that the parameters b and f depend on the strength of group defense of prey species and the death rate of predator species, respectively. Through multiple one-parametric bifurcation diagrams and a two-parametric bifurcation diagram, we have observed that a higher strength of group defense or a larger death rate of predator species can lead to predator extinction in the coexisting dynamics. However, the initial population plays a crucial role in determining the final state of the system. In the case of bistability and tristability scenarios, the system can lead to co-existing steady-state dynamics or co-existing oscillatory dynamics, or a predator extinction state depending on the initial condition.

We have observed long transient dynamics in the temporal system in which the system spends a considerable time around a stationary or oscillatory state before reaching the final state. These dynamics depend on the initial conditions and parameter values. When the group defense parameter b is above the cusp point threshold value, then an increase in predator's death rate f causes appearance of two new coexisting equilibria due to a saddle-node bifurcation. When f is decreased slightly, these two new coexisting equilibria disappear and a narrow region develops between two non-trivial nullclines. When the initial prey or predator population is small, the trajectories are constrained to move through this narrow region leading to the long stationary transition dynamics [see Fig. 5(b)]. Also, a significant change is observed between the population levels in the transient state and the final state. A similar long transient, but oscillatory state, is observed due to saddle-node bifurcation of limit cycle, which is a global bifurcation. In contrast to the long stationary transient discussed above, the final steady state is approximately the average of population over an oscillatory cycle in this case (see Fig. 6).

A homogeneous steady-state of the spatio-temporal system (5), which corresponds to a stable co-existence equilibrium of the corresponding temporal model, can become Turing unstable when the prey-taxis coefficient c crosses a threshold c_T . A Turing solution refers to a stationary periodic

in space solution. A Turing pattern develops and persists in the system when the corresponding temporal model has a single stable co-existing equilibrium point and all the other equilibria are unstable. In this case, we have employed WNA to derive Turing solution for c near c_T and the theoretical findings have been validated using numerical simulations (see Fig. 9). However, if the temporal model has bistability or tristability, then the Turing solution may not persist. We have shown an example (see Fig. 11) where the spatio-temporal system initially approaches a Turing solution but ultimately settles down to predator-extinction state. The reason for this behaviour is the presence of a stable coexisting and a stable predator-free equilibria of the corresponding temporal model. The perturbations around the homogeneous state corresponding to the coexisting equilibrium grow in magnitude and approach a Turing solution, but the system ultimately settles down to the homogeneous state corresponding to predator-free equilibrium. Similar to the temporal transients, the final state of the solution is unpredictable in this case too. Generally, an increase in group defense-induced prey-taxis can lead to predator extinction scenarios from the homogeneous stable coexistence state.

We have also investigated whether the long transient dynamics observed in the temporal model persist in the extended spatio-temporal system. Almost similar long stationary transient dynamics have been found in the presence of diffusion and taxis (see Fig. 12) but the final state consists of a Turing pattern instead of the homogeneous steady state E_1^* . This is due to the taxis parameter c lying in the Turing domain corresponding to the homogeneous state E_1^* . But in the case of transient oscillatory dynamics of the temporal model, the spatio-temporal system does not exhibit any transient dynamics. In this case, the system rapidly reaches the predator extinction homogeneous steady state E_1 (see Fig. 13). Thus, the persistence of long transient dynamics of the temporal model depends on the parameter values of the spatio-temporal model. Another important observation is the appearance of non-homogeneous oscillatory pattern solutions for certain parameter sets lying in the Hopf region (see Fig. 14). Increasing the value of taxis parameter c towards the Turing-Hopf region leads to the appearance of a transient Turing pattern but the system ultimately settles down to the homogeneous steady state E_1 . On the other hand, the non-homogeneous oscillatory pattern solution becomes a homogeneous oscillatory pattern solution with decreasing c towards the interior of the Hopf region.

In summary, the prey-taxis is beneficial to the prey species compared to the predator species. It significantly influences the survival of the predator species. A stable coexisting state of the temporal model can become homogeneous predator-free state in the presence of prey-taxis. Thus, the prey-taxis plays a crucial role in the pattern formation scenario of a spatio-temporal prey-predator system.

Data Availability The authors declare that no experimental data were used in the preparation of this manuscript.

Ethics declarations

Conflict of interest The authors declare that they have no conflict of interest.

Appendix A

Using Gagliardo–Nirenberg inequality [63] with $v \geq 0$, we obtain

$$\begin{aligned} \int_{\Omega} v^q dx &= \int_{\Omega} (v^{\frac{q}{2}})^2 dx \leq a_1 \left(\|\nabla v^{\frac{q}{2}}\|_2^{\frac{2nq-2n}{nq-n+2}} \cdot \|v^{\frac{q}{2}}\|_{\frac{2}{q}}^{\frac{4}{nq-n+2}} + \|v^{\frac{q}{2}}\|_{\frac{2}{q}}^2 \right) \\ &= a_1 \left(\|\nabla v^{\frac{q}{2}}\|_2^{2\theta} \cdot \|v^{\frac{q}{2}}\|_{\frac{2}{q}}^{2(1-\theta)} + \|v^{\frac{q}{2}}\|_{\frac{2}{q}}^2 \right), \end{aligned}$$

where $a_1 > 0$ and $0 < \theta = \frac{nq-n}{nq-n+2} < 1$. Using Young's inequality, we have

$$\|\nabla v^{\frac{q}{2}}\|_2^{2\theta} \cdot \|v^{\frac{q}{2}}\|_{\frac{2}{q}}^{2(1-\theta)} \leq a_2 \theta \|\nabla v^{\frac{q}{2}}\|_2^2 + a_2^{\frac{\theta}{\theta-1}} (1-\theta) \|v^{\frac{q}{2}}\|_{\frac{2}{q}}^2,$$

for any $a_2 > 0$. Thus we have

$$\begin{aligned} \int_{\Omega} v^q dx &\leq a_1 \left(a_2 \theta \|\nabla v^{\frac{q}{2}}\|_2^2 + a_2^{\frac{\theta}{\theta-1}} (1-\theta) \|v^{\frac{q}{2}}\|_{\frac{2}{q}}^2 + \|v^{\frac{q}{2}}\|_{\frac{2}{q}}^2 \right) \\ &= a_1 a_2 \theta \|\nabla v^{\frac{q}{2}}\|_2^2 + a_1 \left(a_2^{\frac{\theta}{\theta-1}} (1-\theta) + 1 \right) \|v^{\frac{q}{2}}\|_{\frac{2}{q}}^2 \\ &= \varepsilon_1 \|\nabla v^{\frac{q}{2}}\|_2^2 + \varepsilon_2 \|v\|_1^q, \end{aligned}$$

for any $\varepsilon_1 > 0$ and for some $\varepsilon_2 > 0$ depending on the ε_1 . Since $\|v\|_1 \leq B$, we obtain

$$\int_{\Omega} v^q dx \leq \varepsilon_1 \|\nabla v^{\frac{q}{2}}\|_2^2 + M \text{ for any } \varepsilon_1 > 0 \text{ and for some } M = \varepsilon_2 B^q > 0.$$

References

- [1] AJ Lotka. Undamped oscillations derived from the law of mass action. *Journal of the American Chemical Society*, 42(8):1595–1599, 1920.
- [2] V Volterra. Variazioni e fluttuazioni del numero d'individui in specie animali conviventi. *C. Ferrari*, 1926.
- [3] PA Stephens, WJ Sutherland, and RP Freckleton. What is the allee effect? *Oikos*, pages 185–190, 1999.
- [4] E Venturino and S Petrovskii. Spatiotemporal behavior of a prey–predator system with a group defense for prey. *Ecological Complexity*, 14:37–47, 2013.
- [5] MT Alves and F Hilker. Hunting cooperation and allee effects in predators. *Journal of theoretical biology*, 419:13–22, 2017.

- [6] Y Kang and L Wedekin. Dynamics of a intraguild predation model with generalist or specialist predator. *Journal of mathematical biology*, 67(5):1227–1259, 2013.
- [7] JD Murray. *Mathematical biology: I. An introduction*. Springer, 2002.
- [8] JD Murray. *Mathematical biology II: spatial models and biomedical applications*, volume 3. Springer New York, 2001.
- [9] AD Bazykin. Structural and dynamic stability of model predator-prey systems. 1976.
- [10] C Arancibia-Ibarra, P Aguirre, J Flores, and P van Heijster. Bifurcation analysis of a predator-prey model with predator intraspecific interactions and ratio-dependent functional response. *Applied Mathematics and Computation*, 402:126152, 2021.
- [11] E Avila-Vales, G Garca-Almeida, and E Rivero-Esquivel. Bifurcation and spatiotemporal patterns in a bazykin predator-prey model with self and cross diffusion and beddington-deangelis response. *Discrete Cont. Dyn. Syst. Ser. B*, 22:717–740, 2017.
- [12] S Dey, M Banerjee, and S Ghorai. Analytical detection of stationary turing pattern in a predator-prey system with generalist predator. *Mathematical Modelling of Natural Phenomena*, 17:33, 2022.
- [13] W Li and S Wu. Traveling waves in a diffusive predator-prey model with holling type-iii functional response. *Chaos, Solitons & Fractals*, 37(2):476–486, 2008.
- [14] W Wang, L Zhang, H Wang, and Z Li. Pattern formation of a predator-prey system with ivlev-type functional response. *Ecological Modelling*, 221(2):131–140, 2010.
- [15] J Huang, S Ruan, and J Song. Bifurcations in a predator-prey system of leslie type with generalized holling type iii functional response. *Journal of Differential Equations*, 257(6):1721–1752, 2014.
- [16] G Seo and G Wolkowicz. Sensitivity of the dynamics of the general rosenzweig-macarthur model to the mathematical form of the functional response: a bifurcation theory approach. *Journal of mathematical biology*, 76:1873–1906, 2018.
- [17] JF Andrews. A mathematical model for the continuous culture of microorganisms utilizing inhibitory substrates. *Biotechnology and bioengineering*, 10(6):707–723, 1968.

- [18] W Sokol and JA Howell. Kinetics of phenol oxidation by washed cells. *Biotechnology and Bioengineering*, 23(9):2039–2049, 1981.
- [19] D Xiao and S Ruan. Global dynamics of a ratio-dependent predator-prey system. *Journal of Mathematical Biology*, 43(3):268–290, 2001.
- [20] HW Broer, K Saleh, V Naudot, and R Roussarie. Dynamics of a predator-prey model with non-monotonic response function. *Discrete and Continuous Dynamical Systems*, 18(2&3):221–251, 2007.
- [21] JS Tener. Muskoxen in canada: a biological and taxonomic review. 1965.
- [22] JC Holmes. Modification of intermediate host behaviour by parasites. *Behavioural aspects of parasite transmission*, 1972.
- [23] AM Turing. The chemical basis of morphogenesis. *Phil. Trans. Royal Society*, 237:37–72, 1952.
- [24] S Kondo and R Asai. A reaction–diffusion wave on the skin of the marine angelfish pomacanthus. *Nature*, 376:765–768, 1995.
- [25] RA Cangelosi, DJ Wollkind, BJ Kealy-Dichone, and I Chaiya. Nonlinear stability analyses of turing patterns for a mussel-algae model. *Journal of Mathematical Biology*, 70(6):1249–1294, 2015.
- [26] A Blagodatski, A Sergeev, M Kryuchkov, Y Lopatina, and VL Katanaev. Diverse set of turing nanopatterns coat corneae across insect lineages. *Proceedings of the National Academy of Sciences*, 112(34):10750–10755, 2015.
- [27] A Ducrots and M Langlais. A singular reaction–diffusion system modelling prey–predator interactions: Invasion and co-extinction waves. *Journal of Differential Equations*, 253(2):502–532, 2012.
- [28] CA Klausmeier. Regular and irregular patterns in semiarid vegetation. *Science*, 284:1826–1828, 1999.
- [29] R Han, S Dey, and M Banerjee. Spatio-temporal pattern selection in a prey-predator model with hunting cooperation and allee effect in prey. *Chaos, Solitons & Fractals*, 171, 2023.
- [30] M Banerjee and S Petrovskii. Self-organised spatial patterns and chaos in a ratio-dependent predator–prey system. *Theoretical Ecology*, pages 37–53, 2011.
- [31] L Zhang, J Liu, and M Banerjee. Hopf and steady state bifurcation analysis in a ratio-dependent predator–prey model. *Commun Nonlinear Sci Numer Simulat*, 44:52–73, 2017.

- [32] JA Sherratt, BT Eagan, and MA Lewis. Oscillations and chaos behind predator–prey invasion: mathematical artifact or ecological reality? *Philosophical transactions of the Royal Society of London. Series B: Biological Sciences*, 352(1349):21–38, 1997.
- [33] KW Foster and RD Smyth. Light antennas in phototactic algae. *Microbiological reviews*, 44(4):572–630, 1980.
- [34] S Ghorai and NA Hill. Penetrative phototactic bioconvection. *Physics of fluids*, 17(7):074101, 2005.
- [35] T Hillen and KJ Painter. A user’s guide to pde models for chemotaxis. *Journal of mathematical biology*, 58(1-2):183, 2009.
- [36] BD Sleeman, MJ Ward, and JC Wei. The existence and stability of spike patterns in a chemotaxis model. *SIAM Journal on Applied Mathematics*, 65(3):790–817, 2005.
- [37] KC Weng, DG Foley, JE Ganong, C Perle, GL Shillinger, and BA Block. Migration of an upper trophic level predator, the salmon shark lamna ditropis, between distant ecoregions. *Marine Ecology Progress Series*, 372:253–264, 2008.
- [38] J Wang, S Wu, and J Shi. Pattern formation in diffusive predator-prey systems with predator-taxis and prey-taxis. *Discrete & Continuous Dynamical Systems-B*, 26(3), 2021.
- [39] B Ainseba, M Bendahmane, and A Noussair. A reaction–diffusion system modeling predator–prey with prey-taxis. *Nonlinear Analysis: Real World Applications*, 9(5):2086–2105, 2008.
- [40] N Sapoukhina, Y Tyutyunov, and R Arditi. The role of prey taxis in biological control: a spatial theoretical model. *The American Naturalist*, 162(1):61–76, 2003.
- [41] MR Myerscough, PK Maini, and KJ Painter. Pattern formation in a generalized chemotactic model. *Bulletin of mathematical biology*, 60(1):1–26, 1998.
- [42] Y Zhang and L Xia. Pattern formation in rosenzweig-macarthur model with prey-taxis. *International Journal of Numerical Analysis & Modeling*, 16(1), 2019.
- [43] G Gambino, MC Lombardo, and M Sammartino. Cross-diffusion-induced subharmonic spatial resonances in a predator-prey system. *Physical Review E*, 97(1):012220, 2018.

- [44] D Luo and Q Wang. Global bifurcation and pattern formation for a reaction–diffusion predator–prey model with prey-taxis and double beddington–deangelis functional responses. *Nonlinear Analysis: Real World Applications*, 67:103638, 2022.
- [45] PK Maini, MR Myerscough, KH Winter, and JD Murray. Bifurcating spatially heterogeneous solutions in a chemotaxis model for biological pattern generation. *Bulletin of mathematical biology*, 53:701–719, 1991.
- [46] A Morozov, K Abbott, K Cuddington, T Francis, G Gellner, A Hastings, YC Lai, S Petrovskii, K Scranton, and ML Zeeman. Long transients in ecology: Theory and applications. *Physics of Life Reviews*, 32:1–40, 2020.
- [47] A Morozov, M Banerjee, and S Petrovskii. Long-term transients and complex dynamics of a stage-structured population with time delay and the allee effect. *Journal of theoretical biology*, 396:116–124, 2016.
- [48] YC Lai and T Tél. *Transient chaos: complex dynamics on finite time scales*, volume 173. Springer Science & Business Media, 2011.
- [49] PR Chowdhury, S Petrovskii, V Volpert, and M Banerjee. Attractors and long transients in a spatio-temporal slow–fast bazykin’s model. *Communications in Nonlinear Science and Numerical Simulation*, 118:107014, 2023.
- [50] L Perko. *Differential Equations and Dynamical Systems*. Springer-Verlag, New York, 2000.
- [51] P Liu, J Shi, and Y Wang. Bifurcation from a degenerate simple eigenvalue. *Journal of Functional Analysis*, 264(10):2269–2299, 2013.
- [52] S Dey, M Banerjee, and S Ghorai. Bifurcation analysis and spatio-temporal patterns of a prey–predator model with hunting cooperation. *International Journal of Bifurcation and Chaos*, 32(11):2250173, 2022.
- [53] S Wu, J Wang, and J Shi. Dynamics and pattern formation of a diffusive predator–prey model with predator-taxis. *Mathematical Models and Methods in Applied Sciences*, 28(11):2275–2312, 2018.
- [54] Y Cai, Q Cao, and Z Wang. Asymptotic dynamics and spatial patterns of a ratio-dependent predator–prey system with prey-taxis. *Applicable Analysis*, 101(1):81–99, 2022.
- [55] JA Carrillo, S Lisini, and E Mainini. Uniqueness for keller-segel-type chemotaxis models. *Discrete and Continuous Dynamical Systems*, 34(4):1319–1338, 2013.

- [56] H Amann. Dynamic theory of quasilinear parabolic equations. ii. reaction-diffusion systems. 1990.
- [57] CV Pao. *Nonlinear parabolic and elliptic equations*. Springer Science & Business Media, 2012.
- [58] M Winkler. Aggregation vs. global diffusive behavior in the higher-dimensional keller–segel model. *Journal of Differential Equations*, 248(12):2889–2905, 2010.
- [59] Y Tao and Z Wang. Competing effects of attraction vs. repulsion in chemotaxis. *Mathematical Models and Methods in Applied Sciences*, 23(01):1–36, 2013.
- [60] Y Tao. Boundedness in a chemotaxis model with oxygen consumption by bacteria. *Journal of mathematical analysis and applications*, 381(2):521–529, 2011.
- [61] AK Drangeid. The principle of linearized stability for quasilinear parabolic evolution equations. *Nonlinear Analysis: Theory, Methods & Applications*, 13(9):1091–1113, 1989.
- [62] E Tulumello, MC Lombardo, and M Sammartino. Cross-diffusion driven instability in a predator-prey system with cross-diffusion. *Acta Applicandae Mathematicae*, 132(1):621–633, 2014.
- [63] A Friedman. Partial differential equations. *Holt, Rinehart & Winston*, 1969.